

The chemical evolution of gas-rich dwarf galaxies

T.I. Larsen¹, J. Sommer-Larsen², B.E.J. Pagel³

¹*Copenhagen University Observatory, Juliane Maries Vej 30, DK-2100 Copenhagen Ø, Denmark (e-mail: thommy_l@astro.ku.dk)*

²*Theoretical Astrophysics Center, Juliane Maries Vej 30, DK-2100 Copenhagen Ø, Denmark (e-mail: jslarsen@tac.dk)*

³*Astronomy Centre, CPES, University of Sussex, Brighton BN1 9QJ, UK (e-mail: bejp@star.cpes.susx.ac.uk)*

Received.....; in original form.....

ABSTRACT

A numerical double burst model of the chemical evolution of gas-rich dwarf galaxies has been developed. The model is fitted to a sample of N/O, O/H, Y and gas fraction observations, where N/O and O/H are the relative abundances by number of nitrogen to oxygen and oxygen to hydrogen, respectively. Y is the abundance by mass of helium. Closed models as well as models including enriched outflow, ordinary outflow and ordinary outflow combined with inflow are considered. The bursts are assumed to be instantaneous but ordered in pairs to explain the scatter in N/O-O/H. The method of gas fraction fitting is revised, and it is found that it is very important to specify whether dwarf irregulars (dIrrs) or blue compact galaxies (BCGs) are considered. Effective enriched winds fail when fitting N/O, whereas closed models, models with ordinary winds or a combination of ordinary winds and inflow are all viable.

Key words: methods:numerical – galaxies:irregular – galaxies:starburst – galaxies:abundances – ISM:H II-regions

1 INTRODUCTION

The chemical evolution of dwarf irregular (dIrr) ^{*} and blue compact emission-line galaxies (BCGs) is of particular interest because a substantial body of observational data is available and some degree of simplicity exists because of the low level of ‘metal’ enrichment and absence of large abundance gradients. Furthermore, their wide range of intrinsic properties makes them suitable objects for testing certain expectations from stellar nucleosynthesis theory and the ‘Simple’ or other models of galactic chemical evolution, although at the same time there are complications associated with inflow of unprocessed material, outflow in homogeneous or selective galactic winds and bursting (or ‘gaspings’) modes of star formation. Chemical evolution models attempt to apply all these concepts to account for the distribution of different elements, notably helium, oxygen and nitrogen, in relation to star formation rates and gas fractions. Because many parameters such as these last two are generally very poorly determined, the most convincing tests come from the comparison of different elements with one another.

Back in the 1970s, Smith (1975), Peimbert (1978) and Edmunds & Pagel (1978) noticed a contribution of primary nitrogen to the N/O ratio in Galactic and extragalactic H II regions with low oxygen abundance and Edmunds & Pagel attributed the existence of scatter in N/O at a given O/H to

the existence of a time delay in primary nitrogen production by intermediate-mass stars, combined with differing effective ages of the underlying stellar populations. Alloin et al. (1979) also noted the primary nitrogen and attributed scatter in N/O to variations in the initial mass function (IMF), whereas Lequeux et al. (1979) in their classic study of helium, nitrogen and oxygen in irregular galaxies and BCGs confirmed the primary nitrogen likewise, but were not convinced that there was any real scatter in their data. The models of Alloin et al. and Lequeux et al. assumed evolution to take place smoothly as a function of time; Matteucci & Chiosi (1983) were the first to incorporate into chemical evolution models for these systems the idea of bursting modes of star formation as previously inferred by Searle & Sargent (1972) and Searle, Sargent & Bagnuolo (1973), and interpreted on the basis of the SSPSF hypothesis by Gerola, Seiden & Schulman (1980). The basic pattern of a primary (constant N/O) pattern at low metallicities in H II regions changing over to a secondary pattern ($N/O \propto O/H$) at higher ones has been confirmed in many more recent investigations (e.g. Vila-Costas & Edmunds 1993; van Zee, Salzer & Haynes 1998).

The chemical evolution of dIrrs and BCGs has been studied in many more recent investigations. Matteucci & Tosi (1985) found good fits to the data with a Salpeter IMF, inflow, homogeneous outflow, bursting star formation and a choice of third dredge-up parameters from Renzini & Voli (1981), attributing scatter in the N/O ratio to variations in M_{up} , the upper limit to the masses of stars undergoing the

^{*} In this paper a dwarf galaxy is defined to have absolute magnitude $M_B \geq -17$.

third dredge-up with hot-bottom burning. Garnett (1990) indicated schematically how the occurrence of bursts could in itself lead to variations in the N/O ratio just as a result of observing systems at different stages in the burst cycle. Pilyugin (1992; 1993) developed similar ideas in quantitative numerical models involving self-enrichment of H II regions and selective galactic winds as well as bursting modes of star formation, and Marconi, Matteucci & Tosi (1994) also developed models with bursts and selective winds, while Carigi, Colín & Peimbert (1999) have investigated similar models, but prefer a ‘bottom-heavy’ IMF similar to one claimed in some globular clusters and giving rise to low true yields. However, part of the motivation for invoking selective winds was the apparent existence of a large dY/dZ ratio suggested by Pagel et al. (1992), which no longer seems valid (Izotov & Thuan 1998), and the scatter in N/O also seems to have been overestimated in those investigations. In this paper, therefore, we investigate the problem again, making use of more recent data and models of stellar nucleosynthesis and exploring in particular the role of mixing processes and of differing burst phases in leading to scatter in the N/O, O/H relation and the relationship between oxygen abundance and gas fraction.

The structure of the article is as follows: Section 2 presents the adopted sample of abundance observations. Section 3 discusses the evolution of H II-regions, wind-driven bubbles and supernova-driven supershells to investigate possible mixing scenarios. This leads to the description of our double-bursting models in section 4. The results of fitting the models to the sample of observations are presented in section 5, and discussed in section 6.

2 THE OBSERVATIONAL DATA

It has been stressed that the sample should consist mainly of BCGs, as these objects are extreme in both star formation rates and metallicity, thus being attractive for a bursting model. Another demand has been to include the most recent data only, in order to get the observations as accurate as possible. Further, a few damped Ly- α systems (DLA) have been included, mainly for the sake of comparison. The motivation for including them is found in the growing opinion that they represent dwarf galaxies in early (high z) stages of evolution. Thus, they may offer some insight into the extreme low-metallicity environment in the early evolution of present-day dwarf galaxies.

The following sample is selected: BCGs and dIrrs from Pagel et al. (1992), BCGs from Izotov, Thuan & Lipovetsky (1997a), the BCG SBS 0335-052 from Izotov et al. (1997b), the BCG IZw18 from Izotov & Thuan (1998), and finally four DLAs from Lu, Sargent & Barlow (1998). From the sample of Pagel et al. (1992) are excluded LMC, NGC5253 and NGC5455/NGC5461 (the last two are H II-regions in the nearby spiral M101), and objects included from one of the other sources. The total sample is shown in fig. 1 for N/O-O/H and fig. 2 for Y-O/H. The N/O abundances seem to have a constant level for $12+\log(\text{O}/\text{H})$ less than 8, implying the major part of the nitrogen to be produced as a primary element. For $12+\log(\text{O}/\text{H})$ higher than about 8, N/O is increasing as a function of metallicity, suggesting the major part of the nitrogen to be secondary. These trends are

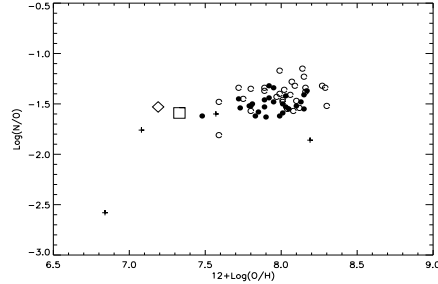


Figure 1. The observational sample used in this paper. The symbols are: diamond=IZw18 (Izotov & Thuan 1998), square=SBS0335-052 (Izotov et al. 1997b), filled circles are BCGs (Izotov et al. 1997a) and open circles are BCGs and dIrrs (Pagel et al. 1992). Finally, the plusses are DLA-systems (Lu et al. 1998).

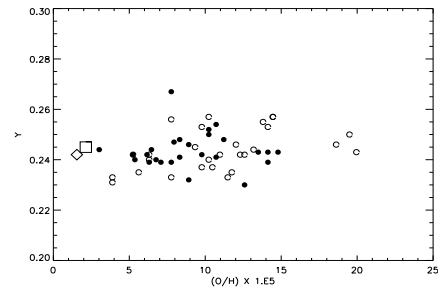


Figure 2. The helium abundance sample. The symbols are as in fig. 1. No DLAs are shown.

wellknown, see e.g. Garnett (1990), Vila-Costas & Edmunds (1993), Pettini, Lipman & Hunstead (1995) and van Zee, Salzer & Haynes (1998a).

Further, the scatter in N/O seems to be significant and our models are based on this assumption. If we fit a straight line to our selected observations, ignoring the DLAs, we find the standard deviation in N/O to be $\sigma=0.11$, which is of the same order of magnitude as the observational uncertainty (Izotov et al. 1997a), but a real scatter is evident in other data from a wider range of sources, see e.g. Kobulnicky & Skillman (1996).

The DLA-systems pose severe problems when observing N and O abundances. Usually the N-lines are occurring on top of underlying absorption, and O-lines are almost always saturated. Because of these difficulties, Lu et al. (Lu et al. 1998) found it useful to use Si or S instead of O, which makes sense as O/Si and O/S are found to be the same as solar in both the Galactic disc and halo as well as in H II-regions in nearby galaxies. The question is whether the abundance ratios are equal to solar at the extreme low metallicity of DLAs. This is by now the largest uncertainty in this method. Thus, in fig. 1, the DLAs are represented by their N/Si and Si/H, assuming that these ratios are equivalent to N/O and O/H. Four systems have been selected from the Lu et al. sample namely those in front of QSO’s 0100+1300, 1331+1704, 1946+7658 and 2343+1232. For the rest of their sample, the quality of the observations restricts the abundance determination to be performed as higher or lower limits. Lu et al. did not make any corrections for dust. However, they noted that the depletion in dust is less than

0.4 dex. Though the observations of the four DLAs are included, they should not be taken too seriously and are not given much attention in this paper.

The helium mass fraction shows a linear dependency on metallicity. This linearity has been used for extrapolation back to $O/H=0$, giving the primordial He abundance. Izotov et al. (1997a) used their observations, included in the present sample as well (filled circles in fig. 2), to obtain 0.243 ± 0.003 , using a linear fit with slope $dY/dZ=1.7 \pm 0.9$ and assuming $Z=20(O/H)$. Error bars are omitted in the figure to keep the clearness. However, the error bars are included in the figures presenting our results in section 5 and show no observational evidence for a scatter. Omitting SBS 0749+568, represented by the isolated point above 0.26 in fig. 2, but including all other galaxies in the sample, a linear least-square fit gives $dY/dZ=2.63 \pm 2.21$, again using $Z=20(O/H)$, and assuming a confidence interval of 95 per cent. This gives a primordial helium abundance $Y_p=0.238 \pm 0.004$, which is consistent with Izotov et al. (1997a) within uncertainties.

3 EJECTA DISPERSAL AND MIXING

Many chemical evolution models assume a one-zone description with instantaneous mixing. Assigning the term one-zone to a BCG seems to be quite a poor approximation, and assuming the mixing to be instantaneous will always be doubtful. However, if we choose to reject the assumptions, we are faced with the problem that no complete theory of mixing is available at present. The problem is that the gas dynamics following a starburst are very complex. The energy input into the ISM comes from photoionization, stellar winds from massive stars followed by SN type II. Different scenarios have been proposed for the dispersal and mixing processes. One of the propositions has been 'self-enrichment', referring to the suggestion that only the H II-region, surrounding the newly formed stellar cluster, is enriched with heavier elements, in particular oxygen. Thus, the observed abundances, using emission lines, may be considerably higher than they would be if observed in the neutral medium. The idea was originally proposed by Kunth & Sargent (1986), suggesting that the enrichment is confined to take place within the Strömgren-sphere. However, the hypothesis is controversial, and a lot of opposing arguments exist. Use of self-enrichment implies the assumption of almost instantaneous mixing within the H II-regions. The problem is that the correlated energy input of SNe changes the physical conditions of H II-regions dramatically. In fact, the density is decreased by a factor $10^3 - 10^6$ and the temperature is increased by a similar factor behind the SN-driven shock front. The observed lines of single or double ionized N and O cannot arise from such extreme conditions. A future project could be X-ray abundance observations. If the observed emission lines cannot form within the superbubble/supershell (hereinafter a 'superbubble' is a wind-driven bubble, while a 'supershell' is a SN-driven shell), they may arise from a region outside the shock front. But according to detailed numerical hydrodynamical models (Tenorio-Tagle 1996), the ejecta will stay within the superbubble/supershell for a large part of their evolution, not enriching the surrounding medium. To test the viability of this statement, a few calculations are pre-

sented below, comparing radii of superbubbles/supershells and radii of H II-regions. Further, observations give evidence against the self-enrichment hypothesis, see e.g. van Zee et al. (1998b), Kobulnicky (1997), Kobulnicky & Skillman (1997) and Kobulnicky & Skillman (1998).

3.1 H II-region evolution

In the following, the radii of H II-regions are calculated for comparison with superbubble/supershell radii. The Strömgren-sphere is defined to be the sphere within which all ionizing photons are absorbed. Thus, setting the flux of ionizing photons equal to the number of recombinations, integrated over the entire Strömgren-sphere gives:

$$\frac{4\pi}{3} R(t)^3 \alpha_B n_e n_p \epsilon = N(t) \quad (1)$$

ϵ is the filling factor, α_B is the recombination rate equal to $2.59 \times 10^{-13} \text{ cm}^3 \text{ s}^{-1}$ ($T=10000\text{K}$) (Osterbrock 1989). n_p and n_e are the number densities of protons and electrons, respectively, and $N(t)$ is the flux of ionizing Ly_e -photons. Assuming that all hydrogen inside of the Strömgren-sphere is fully ionized, $n_e \sim n_p$. The filling factor is an indicator of the uniformity of matter, having a value of 1 when the matter is completely uniformly distributed. A typical value of the filling factor is of the order 0.01 (Kennicutt 1984). The electron density in H II-regions is typically $n_e \sim 100 \text{ cm}^{-3}$ (Izotov et al. 1997a). When inserting these two values into eq. 1, the corresponding rms density is $n_e = 10 \text{ cm}^{-3}$, since $\epsilon = 1$ and $n_e = 10 \text{ cm}^{-3}$ is equivalent to the insertion of the observed values. According to Spitzer (1978, p.251), the first phase in the existence of an H II-region is characterized by an almost static Strömgren-sphere. Henceforth, the radius of this initial sphere will be referred to as 'the initial Strömgren radius', R_0 . During the second phase, the sphere is expanding until the H II-region vanishes. If the flux of ionizing photons is assumed constant for the moment, Spitzer (1978) found the relation

$$R(t) = R_0 \left(1 + \frac{7}{4} \frac{C_{II} t}{R_0} \right)^{\frac{4}{7}} \quad (2)$$

on the basis that the expansion velocity nearly equates the velocity of the associated shock. t is the time since the region started to expand, virtually equal to the age of the burst, and C_{II} is the sound speed in the H II-region, equal to 17 km s^{-1} ($T=10000\text{K}$, $\gamma = 5/3$) (Osterbrock 1989). Eq. 2 is not realistic, though, because the photon flux is decreasing in time. In the following this is taken into account, extending the calculations by Spitzer. Differentiating eq. 1 with respect to time gives

$$\frac{dN}{dt} = 3\beta R^2 \rho_{II}^2 \frac{dR}{dt} + 2\beta R^3 \rho_{II} \frac{d\rho_{II}}{dt} \quad (3)$$

where $\beta = \frac{4\pi}{3} \eta^2 \alpha_B \epsilon$, $n_e = \eta \rho_{II}$, so η gives the relation between the number density of electrons and the mass density. Below it is shown that η cancels in the calculations, so we will not worry about its value. Finally ρ_{II} is the mass density within the H II-region. Consider a shell of ionized gas. Assuming uniform expansion, i.e.

$$\frac{1}{r} \frac{dr}{dt} = \frac{v_i}{R} \quad (4)$$

where r is the comoving radius of the shell and v_i is the velocity of the ionized gas just within the ionization front, assumed to have the same radius R as the Strömgren-sphere. The mass inside the comoving shell is conserved by definition, so $r^3 \rho_{II}$ is constant leading to

$$\frac{1}{r} \frac{dr}{dt} = -\frac{1}{3\rho_{II}} \frac{d\rho_{II}}{dt} \quad (5)$$

Inserting these two equations into eq. 3 gives

$$v_i = \frac{1}{2} \frac{dR}{dt} - \frac{\frac{dN}{dt}}{6\beta R^2 \rho_{II}^2} \quad (6)$$

and $\frac{dR}{dt} = V_i$, the velocity of the ionization front. The physical conditions across the shock, formed ahead of the ionization front may be described by the jump condition

$$\rho_I V_s^2 = p_{II} + \rho_{II} u_s^2 \quad (7)$$

ρ_I being the mass density of the surrounding neutral medium, V_s is the velocity of the shock, p_{II} is the pressure within the H II-region and u_s is the inward velocity of matter with respect to the shock. It has been assumed that the density and pressure between the shock and ionization fronts are the same as within the ionization front, and the pressure of the surrounding neutral medium has been neglected. Assume $V_s = V_i$, so $u_s = u_i = V_i - v_i$, where u_i is the inward velocity of matter with respect to the ionization front. Inserting this and the equation of state $p_{II} = \frac{\rho_{II} C_{II}^2}{\gamma}$

with $\gamma = 5/3$, $\rho_{II} = \sqrt{\frac{N}{\beta R^3}}$ (from eq. 1) and $\rho_I = \sqrt{\frac{N_0}{\beta R_0^3}}$ (i.e. the density before expansion starts) into eq. 7 and 6, one finally arrives at the second order equation

$$\left[\left(\frac{NR_0^3}{N_0 R^3} \right)^{-1/2} - \frac{1}{4} \right] \left(\frac{dR}{dt} \right)^2 - \frac{\frac{dN}{dt}}{6\beta R^2 \rho_{II}^2} \left(\frac{dR}{dt} \right) - \left(\frac{\frac{dN}{dt}}{6\beta R^2 \rho_{II}^2} + \frac{C_{II}^2}{\gamma} \right) = 0 \quad (8)$$

It is straightforward to solve this equation for $\frac{dR}{dt}$, obtaining a differential equation, which is solved numerically, using timesteps equal to 1 Myr. For the calculations we used $n_e = 10 \text{ cm}^{-3}$ ($\beta = 1$) as the initial density. When inserted into the second order equation instead of ρ_{II} , the factor η cancels remembering that it is included in β as well. For every timestep, the density $n_e(t)$ is calculated from eq. 1. The fluxes of ionizing photons are taken from the models by Stasinska & Leitherer (1996), giving the fluxes from 1 Myr to 10 Myr after the burst in intervals of 1 Myr. An instantaneous starburst of mass $10^6 M_\odot$ was assumed, comparable to those used in our model. Further, a Salpeter IMF with the same upper mass limit is used, only demanding a simple scaling from their lower mass $1 M_\odot$ to our lower mass, either 0.1 or $0.01 M_\odot$. If $m_L = 0.1$ the normalization constant is 0.17, see section 4.1. Integration of the IMF yields a mass fraction of 0.39 above $1 M_\odot$, so the adopted fluxes are multiplied by 0.39. Correspondingly, using $m_L = 0.01$ the normalization constant is 0.07, giving a mass fraction of 0.17 above $1 M_\odot$. The decrease of continuum photon flux calculated by Stasinska & Leitherer using their parameter values is shown in figure 3.

R_0 is found from eq. 1 by inserting the initial flux of photons and the initial density $n_e = 10 \text{ cm}^{-3}$. The initial

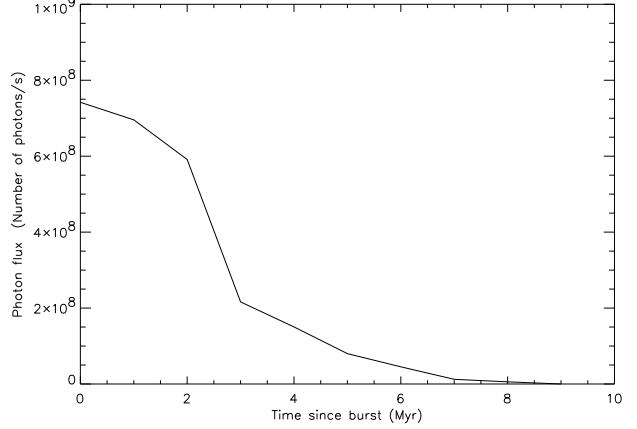


Figure 3. The decrease in ionizing photon flux counted from a starburst event.

flux, $N_0 = N(t = 0)$ is the flux just before the H II-region starts to expand. No information exist on the photon flux before 1 Myr after the burst. Thus, $N_0 = N(1\text{Myr})$ is assumed so R_0 is equal to $R(1 \text{ Myr})$ found from eq. 1. The calculations are performed for both of the IMF's and the results are shown in table 1.

3.2 Supershell evolution

In the case of a single supernova event, it is rather simple to follow the four main evolutionary phases of its remnant analytically. First, the ejecta and the leading shock move almost undecelerated. Second, the velocity of the shock decreases, as a shell of swept-up ISM builds up and grows larger. In this phase, radiation from the hot cavity is not important, and the total energy within the shock is conserved. Third, radiative cooling of all matter within the shock become important. The shell is now driven by the pressure still existing in the cavity. Finally the PdV work from the cavity vanishes, so that the shell is now only being driven by the momentum. At some moment, the velocity of the shell has dropped to a value comparable to the rms velocity of the ISM, thus being non-detectable.

When one deals with the correlated effect of many supernovae, which is the case in starburst galaxies where the number of massive stars is large, additional considerations have to be made, since supernovae keep feeding energy to the cavity for about 50 Myr. The idea with the following calculations is to get a feeling of the timescales and radii of supershells. The analytical expressions from McCray & Kafatos (1987) are adopted to do the simple calculations, and the equations below are taken from their article, unless another reference is given. Strictly speaking, the analytical expressions may be used only if the ambient density is constant. However, the supershell first expands into the wind-driven bubble environment, then into a region with density depending on the H II-region expansion, and finally into a non-expanding region outside the H II-region. Hence, the evolution of the supershell is only followed while it is smaller than the H II-region, and the density within the superbubble is assumed to be the same as outside. This last assumption is not realistic, as the passage of the wind-blown

shock sweeps a large fraction of the gas into a superbubble. Hence, we may expect a more accurate model to show that the supershell reaches the superbubble at an earlier time. The gas gathered by the wind-driven shock cools to form the superbubble after relatively short time

$$t_b = (2.3 \times 10^4 \text{ yr}) n_e^{-0.71} L_{38}^{0.29} \quad (9)$$

(Mac Low & McCray 1988), and the radius of the superbubble is

$$R_s = 269 \text{ pc} (L_{38}/n_e)^{1/5} t_7^{3/5} \quad (10)$$

where L_{38} is the characteristic wind luminosity in units of $10^{38} \text{ ergs s}^{-1}$ and t_7 is the elapsed time since the starburst in units of 10^7 yr . Strictly speaking, the time is counted from the start of superbubble expansion, but since O-stars start their wind-phase soon after the burst, t_7 is counted from the burst. n_e is the matter density within the H II-region, assumed to be homogeneous. The wind luminosity is found in Leitherer & Heckman (1995) from their fig. 55 (instantaneous starburst, metallicity is one tenth of solar, mass of burst is $10^6 M_\odot$, Salpeter IMF with upper limit $100 M_\odot$ and lower limit $1 M_\odot$). At 10^6 yr the wind luminosity is read-off to be $10^{39} \text{ ergs s}^{-1}$. Doing the same IMF scaling as in the photon flux discussion above, $L_{38} = 3.9$ is obtained if $m_L = 0.1 M_\odot$ and $L_{38} = 1.7$ if $m_L = 0.01 M_\odot$. The wind phase is important for as long as O-stars exist ($\approx 5 \text{ Myr}$). However, after about 3 Myr the first supernovae explode and soon dominate the total energy output. The superbubble radius has been calculated 1, 2 and 3 Myr after the burst using eq. 10. The density typical for an H II-region during its early evolution is 10 cm^{-3} , as discussed above.

After 3 Myr, the first SN appear. Hence, the expansion of the supershell is set to start at $t=3 \text{ Myr}$. Strictly speaking, the energy output from supernovae appears as discrete events. However, it can be treated as continuous, as long as the interval between explosions is sufficiently short, at most in the order of 10^5 yr (Tomisaka, Habe & Ikeuchi 1981). If the total mass of the burst is $10^6 M_\odot$, the number of stars with mass greater than or equal to $8 M_\odot$ (lower limit of a SNII progenitor, according to Woosley & Weaver (1986)) may be calculated using our IMF. The result using the $0.1 M_\odot$ lower mass limit is 8145 stars, whereas it is 3452 stars using $m_L = 0.01 M_\odot$. The event lasts for about $5 \times 10^7 \text{ yr}$ so the mean interval between explosions is in the order of $6 \times 10^3 \text{ yr}$ and $1 \times 10^4 \text{ yr}$, respectively. Thus, it is meaningful to assume continuous energy injection. Using this, eq. 10 may be used with just one replacement, namely the insertion of the mean supernova power instead of the wind luminosity. The mean power is calculated by dividing the total SN energy $N_* E_{51} \times 10^{51} \text{ ergs}$ with the total duration of the event. N_* is the number of stars with mass greater than $8 M_\odot$ and E_{51} is the energy in units of 10^{51} ergs . Here, 0.4 is adopted as a representative value, see Woosley & Weaver (1986, their table 1). The energy ejection is assumed not just to be continuous, but also constant in time. This is probably quite a good approximation, see Leitherer & Heckman (1995). The considerations lead to

$$\begin{aligned} R_s &= 97 \text{ pc} (N_* E_{51}/n_e)^{1/5} t_7^{3/5} \\ V_s &= 5.7 \text{ km s}^{-1} (N_* E_{51}/n_e)^{1/5} t_7^{-2/5} \end{aligned} \quad (11)$$

Table 1. H II-regions and supershells

$t(\text{Myr})$	$R_{\text{H II}}(\text{pc})$	$R_s(\text{pc})$	$n_e(\text{cm}^{-3})$
1	209 (158)	56 (47)	10.0 (10.0)
2	222 (172)	85 (72)	8.8 (8.5)
3	233 (184)	108 (92)	7.5 (7.1)
4	239 (189)	123 (103)	4.4 (4.1)
5	245 (196)	186 (157)	3.5 (3.3)
6	250 (201)	237 (200)	2.5 (2.3)
7	255 (206)	282 (238)	1.8 (1.7)

The radii and densities of H II-regions compared to the radii of superbubbles/supershells at different times after the burst calculated with the $m_L=0.1 M_\odot$ cutoff. Values of shell radii typed in bold, are the radii of the superbubbles. For $t>3 \text{ Myr}$, the calculated shell radii are for the supershells. The values for $m_L=0.01 M_\odot$ are given in brackets. The size of the superbubble at 4 Myr after the burst is roughly the same as the size of the supershell, so the supershell reaches the superbubble about 1 Myr after the appearance of the first SNe.

The time of shell formation is given by an expression similar to eq. 9, obtained by replacing the wind luminosity with the mean supernova power.

The density of the H II-region is assumed constant in time and equal to 3 cm^{-3} , a reasonable value during late stage H II-region evolution (see table 1). Eqs. 11 are used in the adiabatic phase only (no cooling), since they implicitly assume that the loss of energy within the shell is negligible. Cooling, and hence energy loss, from the interior becomes important at a time

$$t_c = 4 \times 10^6 \text{ yr} \xi^{-1.5} (N_* E_{51})^{0.3} n_e^{-0.7} \quad (12)$$

At this time, the shell has a radius

$$R_c = 50 \text{ pc} \xi^{-0.9} (N_* E_{51})^{0.4} n_e^{-0.6} \quad (13)$$

found by inserting eq. 12 into eq. 11. ξ is the metallicity in units of the solar metallicity. For the objects in question, $\xi = 0.1$ is a representative value. Even if a small starburst mass of $10 M_\odot$ is assumed and the density of the surrounding medium is 3 cm^{-3} , it turns out that the supershell reaches the end of the adiabatic phase at a time $2.1 \times 10^7 \text{ yr}$ if $m_L=0.1$ is used and $1.6 \times 10^7 \text{ yr}$ if $m_L=0.01$. Hence, the interior of the supershell starts to cool after the H II-region has vanished. This tells us that we may use eqs. 11 to calculate the size of the supershell, as we are only interested in the evolution during H II-region existence. The results are given in table 1.

The measured emission lines may indeed originate in the part of the H II-region that is still outside the superbubble, since the size of the H II-region always exceeds the size of the superbubble as seen in table 1. It also exceeds the size of the supershell until 6 Myr after the burst, though only significantly within the first 5 Myr. The above calculations do not prove that the emission lines arise outside the superbubble/supershell - they just confirm that it is a possibility. If emission lines really are measured this way, they are not affected by enrichment from the present burst, thus opposing self-enrichment.

3.3 Propagating star formation

Propagating star formation means that the energy deposited in the ISM by an evolving star formation event, is initiating

new star formation. As a supershell grows, it will become Rayleigh-Taylor unstable and fragments. The situation has been treated by Elmegreen (1994), who found an expression for the timescale of cloud-collapse in the supershell:

$$t_{cloud} = 103 \left(\frac{n_0 \mathcal{M}}{\text{cm}^{-3}} \right)^{-1/2} \text{Myr} \quad (14)$$

where \mathcal{M} is the expansion speed of the shell divided by the rms velocity dispersion in the shell. For an adiabatic shell, \mathcal{M} is equal to 1.8 (Elmegreen 1994). If $n_0 = 10 \text{ cm}^{-3}$, this gives the result that star formation is expected to start not earlier than ~ 24 Myr after shell formation. On the other hand, if $n_0 = 3 \text{ cm}^{-3}$ as used in the calculations above for a typical density in the late stages of H II-region evolution, the timescale is more like 44 Myr. The mass of the supershell is given as

$$M = \rho_0 V_{ss} \approx 1.3 n_0 m_p \frac{4\pi}{3} R^3 \quad (15)$$

assuming all of the ISM originally within R to be incorporated in the shell. ρ_0 is the mass density of the ambient medium, V_{ss} is the volume occupied by the hot phase within the supershell, m_p is the proton mass and 1.3 is the approximate mass per particle in units of the proton mass. The radius is of the order a few 100 pc as shown above, so eq. 15 gives a shell mass of the order $10^6 M_\odot$. Hence the induced star formation is of the same order of magnitude as the original central burst.

Observational indications on the existence of star forming supershells are numerous. One recent example is NGC 2537 included in the sample of Martin (1998). In H_α , it shows a very clear spherical distribution of starformation sites. As a curiosity, it may be mentioned that Mori et al. (1997) calculated the effects of star formation in an expanding supershell, using a 3-D hydrodynamical code including a dark matter halo. The results were in remarkable accordance with available observations of dE's, such as exponential surface brightness profile, positive metallicity gradient and inverse color gradients.

If the ejected metals from the central burst mix with the material of the supershell, the H II-regions of the induced burst will show abundances differing from the central H II-region. Although there have been some doubt whether the metals are allowed to mix into the supershell (Tenorio-Tagle 1996), and if so when this will happen, we have been inspired by this possibility to let our model have a double burst nature.

4 THE MODEL

We have designed a model to fulfil certain demands, namely that the observed trend of constant N/O for low metallicities and increasing N/O for higher metallicities should be reproduced and also that the observed scatter in N/O should be explained. Fixing all the parameters by fitting the N/O-O/H evolution, the model should also be able to explain the observed helium mass fraction as a function of O/H and O/H as a function of gas fraction.

The included elements are H, He, C, N, O. The production of N is still a hot topic, since the degree of primary production at various metallicities is unclear. Further, N

is produced mainly by intermediate mass stars while O is produced by massive stars, making it necessary to include stellar lifetimes. However, the inclusion of both N and O provides the opportunity of constraining stellar parameters and mixing scenarios.

To account for the scatter in N/O, it is suggested that the bursts are instantaneous and ordered in pairs, hence using the delay between the ejection of N and O. The principle of time delay was used by Garnett (1990), though employing single bursts only. It is doubtful whether single bursts produce scatter, since at least some abundance observations have to be done at the time of N-release. However, this is between two bursts, where no giant H II-regions are present, providing no possibility for abundance observations by emission lines. Single bursts may produce scatter only if IMF parameters or enriched wind efficiencies vary from galaxy to galaxy. However, there is no indication of IMF variations, and the existence of enriched winds, on the whole, is questionable, and may be important in extreme low-mass galaxies only - see below. Double bursts produce the scatter quite naturally: It was found reasonable above that a localized burst results in another burst, this time in the expanding supershell, surrounding the original burst. The timescale for star formation in the supershell is found to be $\gtrsim 2.4 \times 10^7$ yr, comparable to the timescale for O-ejection, but shorter than the timescale for N-ejection, hence producing the desired scatter.

In our model we assume that the very first burst is a single one, all other bursts appear in pairs. The interburst period between the two bursts of a pair is tuned to give maximum scatter, found below to be 30 Myr. The time between two pairs is set to 1 Gyr.

4.1 The IMF

The IMF used throughout this paper is the single-power Salpeter-IMF:

$$\phi(m) = \phi_0 m^{-2.35} \quad (16)$$

(Salpeter 1955). ϕ_0 is the normalization constant, found by $\int_{m_L}^{m_U} m \phi(m) dm = 1$. Using a lower mass cutoff $m_L = 0.1 M_\odot$ and an upper mass limit $m_U = 100 M_\odot$, ϕ_0 is equal to 0.17. These limits are standard values, very often used in the literature. A Salpeter IMF still fits the observations (above about $1 M_\odot$) quite well despite of its age and simple appearance (Leitherer 1998).

The lower-mass cutoff is an important parameter because the yield from a generation of stars is a function of the adopted lower mass. The reason is that stars less massive than $\sim 1 M_\odot$ do not eject metals, thus locking-up all the material from which they are formed. Hence, lowering the lower-mass cutoff implies a lower recycling fraction, giving a lower yield. As will be apparent from our results, it becomes attractive to invoke another value of m_L namely $0.01 M_\odot$. In this case the normalization constant is found to be 0.07. Thus, the yield will be a factor 2-3 lower when using the lower cutoff.

Throughout this paper, a metallicity invariant Salpeter IMF has been used, since there are at present several observational indications of an abundance invariance (Wyse 1998;

Massey 1998). The number of stars with mass $[m_1, m_2]$ is given by

$$\begin{aligned}
 N([m_1, m_2]) &= \phi_0 M_{burst} \int_{m_1}^{m_2} m^{-2.35} dm & (17) \\
 m_1 &= m_j - \frac{\Delta m}{2} \\
 m_2 &= m_j + \frac{\Delta m}{2}
 \end{aligned}$$

where M_{burst} is the mass of a burst, i.e. the mass of gas turned into stars. The stellar mass grid may be as fine as one wishes. For use in the present model, a grid of 60 different stellar masses has been adopted, since this was found to give sufficient mass resolution for the present purpose.

The mass of each burst may be constrained by the available observations of SFRs. The SFR for BCGs is typically $0.1 - 1 M_\odot \text{yr}^{-1}$. For the mean SFR of a double burst to be within this range, the masses of the bursts may be estimated from $M_{burst}(1) + M_{burst}(2)/t_{ib} \sim 0.1 - 1$, where t_{ib} is the time between the two bursts of a pair. If $t_{ib} = 3 \times 10^7$ yr, and assuming $M_{burst}(1) \sim M_{burst}(2)$, this gives $M_{burst} \sim 1.5 - 15 \times 10^6 M_\odot$, in agreement with Marlowe et al. (1995, their table 7).

4.2 The equations

The calculation of abundances is carried out just before every burst. The reason for doing this is simply that we wish to compare with the observed abundances, being measurable in H II-regions only. The adopted equations are described in the following. The notation is similar to the one in Pilyugin (1993). The first step is to calculate the masses of each element present in the gas phase just before every burst. For the j^{th} burst:

$$\begin{aligned}
 M_i(t_j) &= M_i(t_{j-1}) - \Delta M_{j-1} X_i(t_{j-1}) & (18) \\
 &- \Delta W_i(t_{j-1}) + \Delta W^{Inf}(\tau_{j,j-1}) X_i^{Inf} \\
 &+ \sum_{k=1}^{j-1} \Delta M_k (Q(\tau_{j,k}) - Q(\tau_{j-1,k})) X_i(t_k) \\
 &+ \sum_{k=1}^{j-1} \Delta M_k (Q_i(\tau_{j,k}) - Q_i(\tau_{j-1,k}))
 \end{aligned}$$

t_j refers to the time just before the j^{th} burst. $X_i(t_k)$ is the abundance of element i just before the k^{th} burst. $\tau_{j,k}$ is defined as $t_j - t_k$, so it is the time elapsed since the k^{th} burst. Thus the element yields from stars with lifetimes shorter than $\tau_{j,k}$ has to be included in the two summations. $Q(\tau_{j,k})$ is the mass fraction of gas ejected from the k^{th} generation of stars, just before starburst j . The composition is left unchanged by stellar nucleosynthesis, thus being the same as in the gas from which the stars were formed. $Q_i(\tau_{j,k})$ is correspondingly the mass fraction ejected of element i , but newly synthesized. It is clear from this notation that $Q(\tau_{j,j}) = Q_i(\tau_{j,j}) = 0$, since stellar lifetimes are finite. The first term on the right side is the mass of element i just before the $(j-1)^{th}$ burst. The second term is the mass of element i that has been turned into stars at burst $j-1$. The first summation term is the mass of element i ejected, without being changed, by the k^{th} burst in the period between

the $(j-1)^{th}$ and j^{th} burst. The second summation term is corresponding to the first one, except for the fact that the mass of element i was newly synthesized.

$\Delta W_i(t_{j-1})$ is the mass of element i , leaving the galaxy as a result of starburst $j-1$. This term consists of two parts: The part belonging to the ordinary wind, and the one corresponding to the enriched wind. Thus, the wind term may be written as

$$\begin{aligned}
 \Delta W_i(t_j) &= W_{ISM} \Delta M_j X_i(t_j) & (19) \\
 &+ W_{SN} (Q_i(t_w) + Q(t_w) X_i(t_j)) \Delta M_j
 \end{aligned}$$

(Pilyugin 1993). W_{ISM} and W_{SN} are the efficiencies of the ordinary and enriched winds, respectively. Both efficiencies are zero if the model is closed. The physics behind enriched winds is based on the principle that the supershell following a burst, breaks up, allowing the hot ejecta to blow out and escape from the galaxy. It is assumed that the wind is caused by supernovae type II, so the end of the wind phase t_w is the lifetime of the least massive star exploding as a SNII, which is set to $8M_\odot$, consistent with the mass adopted for our supershell calculations. Hence, for stars with masses above this limit, a fraction W_{SN} of the ejected mass of element i is leaving the galaxy. For stars less massive, $W_{SN} = 0$. It is important to notice, in accordance with the physics involved that this efficiency factor is the same for all elements considered, but since oxygen is dominating the ejecta from SNII, the winds will be enhanced in oxygen.

The other possibility is ordinary galactic winds, arising as a consequence of a general heating of the ISM, causing a fraction to leave the galaxy, i.e. the composition of the gas leaving the galaxy is the same as the composition of the ISM. The first term of eq. 19 is the instantaneous-burst representation of Hartwick-outflow (Hartwick 1976), giving a mass-loss proportional to the burst mass. By multiplying the mass of the wind with the fraction of the i^{th} element in the ISM, taken just before the burst that is responsible for the wind, one obtains the mass removed of element i due to an ordinary wind. W_{ISM}, W_{SN} and the burst masses are treated as free parameters, though one restriction is made, namely that the yields of the first burst should be sufficient to place the second burst *approximately* at the abundances of IZw18.

$\Delta W^{Inf}(\tau_{j,j-1}) X_i^{Inf}$ is the increase in mass since the last burst of element i in the ISM due to inflow of gas. The composition of the infalling gas, given by X_i^{Inf} , is taken to be primordial. The inflow rate is given by

$$\dot{M}(t) = \frac{M_0}{\tau_{inf}} e^{-t/\tau_{inf}} & (20)$$

(Lacey & Fall 1985; Sommer-Larsen & Antonuccio-Delogu 1993). M_0 is the total mass accreted for $t \gg \tau_{inf}$ and τ_{inf} is the accretion timescale. The mass accreted at time t is found by integrating eq. 20 from 0 to t finding $M(t) = M_0(1 - e^{-t/\tau_{inf}})$, finally giving

$$\Delta W^{Inf}(\tau_{j,j-1}) \equiv M(t_j) - M(t_{j-1}) & (21)$$

$$= M_0(e^{-t_{j-1}/\tau_{inf}} - e^{-t_j/\tau_{inf}}) & (22)$$

This is unfortunately giving two free parameters further, namely τ_{inf} and M_0 . In models not including inflow $\Delta W^{Inf}(\tau_{j,j-1}) = 0$. The mass of gas just before starburst

number j is

$$\begin{aligned} M_g(t_j) &= M_g(t_{j-1}) - \Delta M_{j-1} - \Delta W(t_{j-1}) \\ &+ \Delta W^{Inf}(\tau_{j,j-1}) \\ &+ \sum_{k=1}^{j-1} \Delta M_k(Q(\tau_{j,k}) - Q(\tau_{j-1,k})) \end{aligned} \quad (23)$$

Finally the mass of the entire galaxy is

$$M_{dw}(t_j) = M_{dw}(t_{j-1}) + \Delta W^{Inf}(\tau_{j,j-1}) - \Delta W(t_{j-1}) \quad (24)$$

For the closed models $M_{dw}(t_j) = M_{dw}(0)$.

Q_i and Q are adopted from models of stellar evolution as described in section 4.3. However, $Q_H(t)$ is calculated from

$$\sum_{i=H,He,C,N,O} Q_i(t) = 0 \quad (25)$$

assuming all newly consumed H to go into the production of He, C, N and O. This simplification is realistic because the involved elements are by far the most important.

From the above equations, it is now possible to calculate the abundances by mass in the ISM, just before a new burst:

$$X_i(t_j) = \frac{M_i(t_j)}{M_g(t_j)} \quad (26)$$

However, the observed abundances are not given by mass, but by number. The abundance by number of, say $O(t_j)$ relative to $H(t_j)$ is

$$\frac{O}{H}(t_j) = \frac{M_O(t_j)}{M_H(t_j)} \frac{A_H}{A_O} \quad (27)$$

where A represent the atomic masses and M is the gas phase masses calculated by eq. 18.

In the calculations it is assumed that the ejecta mix into the entire interstellar medium before the new burst appear. It should be noted that this assumption is doubtful for the short interburst period between the two bursts of a pair. The fact that the metallicity of second generation stars is slightly higher, is included in the sense that the adopted yields are metallicity dependent. The calculations are terminated if the amount of gas is insufficient for a new burst, or the age of the dwarf galaxy is more than 15 Gyr.

The initial conditions to be put into the equations are the following. The very first burst (the single burst) takes place at primordial gas composition, i.e. $Z=0$, $X_{He}=0.243$ (Izotov et al. 1997a), $X_H=0.757$, $X_C=X_N=X_O=0$.

Before the first burst, the galaxy consists of gas only. Hence, the total mass of the galaxy is equal to the mass of gas, in all calculations adopted to be $10^8 M_\odot$. However, the situation is a little different for the inflow models. In this case, the initial mass of a galaxy is adopted to be zero. Gradually, the galaxy increases its mass by inflow of primordial gas, until the gas mass reaches a limit, sufficient to start the first burst. To be consistent, this mass limit has been adopted to be $10^8 M_\odot$. So the only difference from models not including inflow is that the first burst is delayed by the time it takes to build up a sufficiently large gas cloud.

4.3 The adopted yields and their implementation

Since the present models follow the evolution from the very first burst at $Z=0$ to about solar metallicity, metallicity-

dependent yields have been adopted. The Renzini & Voli (1981) yields for low- and intermediate mass stars are the most widely used for the purpose of chemical evolution modelling. Their strength is that they are giving the yields for several choices of convection and wind parameters. Furthermore they give the primary yield of nitrogen (and ^{13}C) separately, which is very important for our purpose. Indeed, one of the major problems to solve for low metallicity objects is the extent of primary produced N, compared to the secondary production. Marigo, Bressan & Chiosi (1998) made also a separation between primary and secondary production in the mass interval $4-5M_\odot$. The question whether stars more massive than $5M_\odot$ produce primary N is controversial. The question is whether it is necessary at all to introduce such a source for primary N production. This is one of the questions we address in this paper. The yields by van den Hoek & Groenewegen (1997), also for low- and intermediate mass stars, do **not** include separate results for primary nitrogen, so the yields given are a mixture of primary and secondary components. This is the reason, why we have not adopted their yields for more than just a reference, see section 5.

For use in the models, yields are selected in a consistent way, i.e. yields from Geneva tracks (Maeder 1992) and yields from Padova tracks (Marigo, Bressan & Chiosi 1996; Marigo et al. 1998; Portinari, Chiosi & Bressan 1997) are kept in separate sets of yields. The adopted yields are organized as shown in table 2. Note that not all yields in sets 1, 2a and 2b are deduced directly from the Geneva tracks, as van den Hoek & Groenewegen (1997), Renzini & Voli (1981) and Woosley & Weaver (1995) use different indirect methods.

The problem is to calculate the Q and Q_i terms just before every burst, given the IMF and the ages of the previous bursts from which the stars eject the elements. The mass ejected of an element i , at a time τ after a burst is calculated as a sum of contributions from each star down to a stellar mass m_τ , corresponding to a lifetime τ . The lifetime of each star is found by linear Lagrange interpolations in both mass and metallicity between the values given by the stellar tracks. The following expression is used for calculating Q_i

$$Q_i = \sum_{m_j > m_\tau} q_i(m_j) N(m_j) \quad (28)$$

where $N(m_i)$ is the number of stars with mass m_i , found with the adopted IMF, and $q_i(m_i)$ is the mass ejected of element i from stars having this mass. The q_i s are found from the references in table 2 in two steps. First, a linear interpolation is performed between the values for the available metallicities. If the metallicity is lower than the metallicities, for which the yields are known, primary and secondary components of N are treated differently. The yields for primary elements are taken to be equal to the yields at the lowest metallicity with known yields, except for set no. 3, in which the primary N is obtained by extrapolating linearly from the two metallicities with known yields. For this set, an extrapolation should be more correct than just assuming the yield to be constant below the range of metallicities covered by the yield sources, since the range does not extend below $Z=0.008$ for the critical mass interval $4 - 5 M_\odot$. The price to pay is an extrapolation reaching far beyond the covered metallicity range. Note that stars with masses less than 4

Table 2. The organization of the adopted yields.

set no.	Mass range (M_{\odot})	Metallicities	Elements	Reference
1	9-100	0.001,0.02	He,C,O, m_{rem}	M92 (large mass-loss)
	9-40	0.002,0.02	Nsec	WW95
	0.8-8	0.001,0.004, 0.008,0.02	He,C,N, O, m_{rem}	HG97
2a	9-100	0.001,0.02	He,C,O, m_{rem}	M92 (large mass-loss)
	9-40	0.002,0.02	Nsec	WW95
	1-8	0.004,0.02	He,C,Nprim, Nsec,O, m_{rem}	RV81
2b	As 2a, but small mass-loss for stars with $M > 9M_{\odot}$			
3	6-100	0.0004,0.004, 0.008,0.02	He,C,Nsec,O, m_{rem}	P97
	4-5	0.008,0.02	He,Csec,Cprim, Nsec,Nprim,Osec, Oprim, m_{rem}	M98
	1.046-3	0.008,0.02	He,C,Nsec,O, m_{rem}	M96

Sources: M92:(Maeder 1992, His tables 4,5 and 6), WW95:(Woosley & Weaver 1995, their tables 5A,5B,10A and 10B), HG97:(van den Hoek & Groenewegen 1997, their tables 13,17,35 and 38. Tables 13 and 17 are using a wind parameter $\eta=4$ for $Z=0.008$ and $Z=0.02$. For $Z=0.001$ (table 38) and $Z=0.004$ (table 35), η is 1 and 2 respectively), RV81:(Renzini& Voli 1981, their tables 3a,3d,3h and 3i. For all tables, $\eta=0.333$. For tables 3a ($Z=0.02$, $Y=0.28$) and 3h ($Z=0.004$, $Y=0.232$), α is equal to 0. In the two other tables, α is 1.5, and $m_{HBB}=8 M_{\odot}$), P97:(Portinari et al. 1998, their tables 7 and 10), M98:(Marigo et al. 1998, their tables 4 and 5, $m_{HBB}=5 M_{\odot}$) and M96:(Marigo et al. 1996, their tables 4 and 5)

M_{\odot} or larger than the upper mass for hot bottom burning (free parameter in the model for set 2a and 2b, and $5 M_{\odot}$ for set 3) are only producing secondary N. The secondary N yield is interpolated between the lowest metallicity with known yields and $Z=0$, since the yield of secondary N is 0 at $Z=0$, according to the definition of secondary production. For H, He, C and O the yields interpolated/extrapolated are the sum of primary + secondary yields. This is without influence on the results.

Second, the yields are interpolated linearly with respect to initial stellar mass, finally giving the q_i s. For 2a and 2b, the mixing length parameter α , defined as the convection mixing length divided by the pressure scale height, is a free parameter. We know the yields for two different values of α from Renzini & Voli (1981), namely $\alpha=0$ and $\alpha=1.5$. Thus when implementing the yields, the q_i s are found in three steps. Before the two steps described above are carried out, the yields given in the mass interval $4 M_{\odot}$ to the upper mass of HBB, m_{HBB} , variable between 5 and $8 M_{\odot}$, are linearly interpolated with respect to α .

The implementation of the mass ejected unprocessed is very similar. The expression for the total mass ejected since the starburst is written as

$$Q = \sum_{m_i > m_{rem}} (m_i - m_{rem}) N(m_i) \quad (29)$$

m_{rem} is the mass of the stellar remnant (white dwarf, neutron star or black hole). Again the value of m_{rem} is extracted from the sources by linear interpolation, first with respect to metallicity, then between initial stellar masses.

Table 3. The true yields and return fractions for the sets in use.

	Z	p_{He}	p_O	R
Set 2a	0.001	0.032 (0.011)	0.020 (0.007)	0.274 (0.116)
	0.02	0.031 (0.011)	0.008 (0.003)	0.283 (0.120)
Set 2b	0.001	0.032 (0.011)	0.020 (0.007)	0.274 (0.116)
	0.02	0.024 (0.008)	0.014 (0.005)	0.282 (0.119)
Set 3	0.001	0.076 (0.026)	0.014 (0.005)	0.279 (0.118)
	0.02	0.096 (0.032)	0.014 (0.005)	0.299 (0.127)

The values given are for the high low-mass cutoff. Numbers in brackets are for the low cutoff. Note that the He yields for set 3 are higher than for the other sets by a factor of about 3. The O yields are generally quite robust, though the yields of set 2a at solar metallicity ($Z=0.02$) are lower by a factor of about 2, compared to the other O yields at this metallicity. R is the return fraction.

It is very useful to calculate the true yields of selected elements because they allow for an easy comparison between the nucleosynthetic outcome of different stellar models. The true yield of an element is defined to be the mass of an element ejected from a star generation, divided by the fraction locked up in stellar remnants and low-mass stars. The total mass ejected of an element, e.g. O is given by $\sum_{m_i} q_O(m_i) N(m_i)$, where $q_O(m_i)$ is found from the sources following the process described above. The lock-up fraction is equal to $1-R$, where R is the return fraction, i.e. the mass ejected in units of the total mass of the burst Q/M_{burst} . The resulting true yields are given in table 3 for He and O, as

Table 4. The stellar lifetimes for the two stellar tracks.

M	Geneva		Padova	
	Z=0.001	Z=0.02	Z=0.0004	Z=0.02
M_{\odot}				
100	3.21E+06	3.09E+06	3.38E+06	3.39E+06
60	4.08E+06	3.89E+06	4.19E+06	4.12E+06
40	5.34E+06	4.79E+06	5.44E+06	5.12E+06
20	1.02E+07	8.96E+06	1.05E+07	9.15E+06
15	1.45E+07	1.28E+07	1.52E+07	1.33E+07
6	1.00E+08	1.08E+08	7.62E+07	7.45E+07
4	3.41E+08	4.40E+08	1.82E+08	2.03E+08
2	1.99E+09	2.91E+09	1.08E+09	1.21E+09
1	1.07E+10	1.74E+10	7.13E+09	1.03E+10

we shall need these quantities later. Note that the true He yields for set 3 are higher than those of 2a and 2b, in particular at the higher metallicities. Note also the lower yields, when using $m_L=0.01$, by a factor of ~ 2.8 .

4.4 Stellar lifetimes and element timescales

In the case of set no. 1, 2a and 2b, the stellar lifetimes are adopted from Schaller et al. (1992) (Geneva-tracks), while in set no. 3 they are from Portinari et al. (1998) (Padova-tracks). To compare the two sources, lifetimes are shown for some selected metallicities and masses in table 4. It is possible directly to compare the stellar lifetimes at solar metallicity. Low- and intermediate mass stars seems to have shorter lifetimes using the Padova-tracks (between ~ 40 to ~ 70 per cent), while the opposite is true for massive stars (but $\lesssim 10$ per cent longer). This age difference may be a result of different stellar wind-efficiencies, and the inclusion of overshooting in the Padova-tracks.

By combining our knowledge of stellar yields with the respective lifetimes as function of mass, we obtain information on the ejection timescales of different elements. For the present purpose, it is the difference between the timescales of N and O ejection that is particularly interesting, since the time when the ejected N/O has its minimum is equal to the time, where the second burst of a pair should appear if maximum scatter is to be obtained. The timescales are found for a fixed metallicity at which the ejected masses of O and N of one burst are calculated in small timesteps (of the order of $\sim 10^6$ yr) until all stars down to $1 M_{\odot}$ have ended their life cycle. The time evolution of the element ejection has been calculated for set no. 2a and 3 for two metallicities. Fig. 4 shows the timescales for set 2a. The results for set 3 are very similar.

The production of N in massive stars is different for the two metallicities. For solar metallicity, it is released much faster for $\alpha=1$, i.e. by more massive stars. This is only secondary N though, since the contributors have lifetimes shorter than 50 - 80 Myr, hence being more massive than $8 M_{\odot}$ (compare with the stellar lifetimes given in table 4). For set 2a, it is not surprising that the ejection timescale of N is much shorter at low metallicity if $\alpha=0.0$ (dashed lines in fig. 4) than if $\alpha=1.0$, because no primary nitrogen is ejected from intermediate mass stars when $\alpha=0.0$. The major N production sets in at about 100 Myr at the low metallicity. For solar metallicity a large fraction is produced within the first 50 Myr, about 40 (2a) to 60 per cent(3).

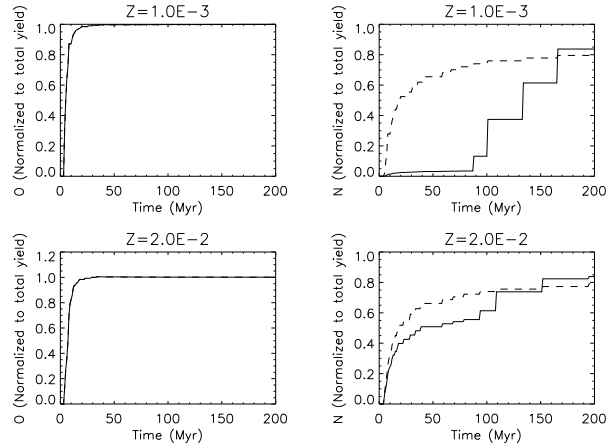


Figure 4. The time evolution of O and N ejection after an instantaneous burst using set 2a, at two different metallicities, and two different values of α . Dashed lines correspond to $\alpha=0$, solid lines to $\alpha=1$. O is to the left and N to the right. The y-axis is the mass ejected of N or O, in units of the total mass ejected of N or O when all stars have ended their life. The step-like appearance of the curves is a consequence of the combined action of discrete stellar masses and finite timesteps. $t=0$ is the time of the burst.

Almost all of the oxygen is produced in $\lesssim 30$ -40 Myr for all sets and metallicities.

Hence, in order to choose the interburst period between the bursts of a pair, a minimum value of N/O would appear somewhat between 30 and 80 Myr for the low metallicity and between 30-40 Myr for the high metallicity. If a choice has to be made, 30 Myr would be the best to make, since, in general, it is easier to reproduce scatter at low metallicities due to the relative effect of ejected metals to metals already present in the interstellar medium. Following this conclusion, the time between the two bursts of a pair is set to 30 Myr.

5 RESULTS

The model is applied to fit the observations in the N/O-O/H plane with the use of the yields in table 2. The accompanying results on Y-O/H and O/H vs. gas fraction are displayed as well. The order of presentation starts with the results of the closed model.

5.1 The closed model

The closed model has been applied to all of the yield sets. In most plots, the IMF with $m_L=0.1$ has been used. For those employing the 0.01 low-mass limit, it is mentioned separately in the text. It is not necessary to do all calculations for both IMF's, since the results are the same, except for the gas fractions. For all elements, the only difference is a lower yield using the low value of m_L , hence more massive bursts are needed to produce the same abundances as when the higher low-mass limit is used. This statement is confirmed in the following.

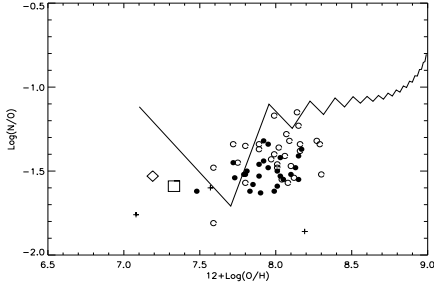


Figure 5. Results for a closed model using yield set no. 1 and $m_L = 0.1 M_\odot$. The following parameters were adopted: Period between pair of bursts is 1 Gyr and the short interburst periods are 30 Myr. The mass of the first burst is $1 \times 10^6 M_\odot$ and the masses of the successive bursts are $3 \times 10^6 M_\odot$. The observations shown are the same as in fig. 1.

5.1.1 N/O-O/H

Fig. 5 shows the evolutionary path of a double-bursting dwarf galaxy, as it has been calculated by the model using yield set 1. The point where the evolutionary path starts (at $12+\log(\text{O}/\text{H}) \sim 7.1$) is where the second burst appears, 1 Gyr after the first burst. The next point is where the third burst would be observed, 30 Myr after the second burst. Thus, the upper points of the saw-tooth pattern are corresponding to the first bursts of each pair, and the lower points to the second pair-bursts. The scatter is more pronounced at low metallicities because the mass of O ejected relative to the one already present in the ISM is higher, the lower the metallicity. It is clear from this figure, why set no. 1 is used as a reference only. The level of N/O is much too high, in particular at low metallicities. The only way one can lower the ratio is by assuming a top heavy IMF, since the yields from van den Hoek & Groenewegen (1997) do not allow for changing the convection parameters or provide possibilities for distinguishing between primary and secondary components. Thus, it is not possible to scale the secondary components separately to $Z=0$. Further, neither outflow nor inflow is able to cure the problem, in particular not if selective winds are considered, since this would increase N/O even more.

It is interesting to note that the parameters (convection, wind etc.) used to fix the yields in van den Hoek & Groenewegen (1997) have been found by using a synthetic model on AGB stars in the LMC and in the Galactic disc. The LMC is not represented in fig. 5, but according to Pagel et al. (1992) $12+\log(\text{O}/\text{H}) = 8.36$ and $\log(\text{N}/\text{O}) = -1.22$ for LMC, which is fitted fairly well after 4 pairs of bursts (but may be fitted by 2 pairs of bursts if the mass of each burst is larger), thus being consistent. The problem seems to arise at lower metallicities.

Next, set 2a is applied (fig. 6). The upper mass limit of hot bottom burning (HBB) is set to $m_{\text{HBB}} = 5M_\odot$, compatible with set no. 3. In this case, a value of $\alpha=1.1$ is necessary to obtain the right level of N/O. A larger value of the convection parameter would produce too much primary N and vice versa. Both theoretical predictions and observations of AGB stars in the Large Magellanic Cloud are suggesting a level of HBB, roughly corresponding to $\alpha=2.0$ (van den Hoek & Groenewegen 1997, and references therein), which

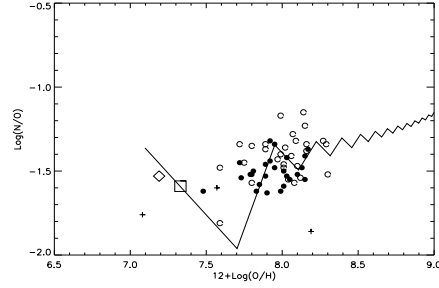


Figure 6. Results for a closed model using yield set no. 2a and $m_L=0.1$. The following parameters are used: Period between pair of bursts is 1 Gyr and the short interburst periods are 30 Myr. The mass of the first burst is $1 \times 10^6 M_\odot$ and the masses of the successive bursts are $3 \times 10^6 M_\odot$. Finally, the upper mass of hot bottom burning, m_{HBB} , is $5M_\odot$. For this plot, $\alpha = 1.1$ is used, since this value places N/O at the right level.

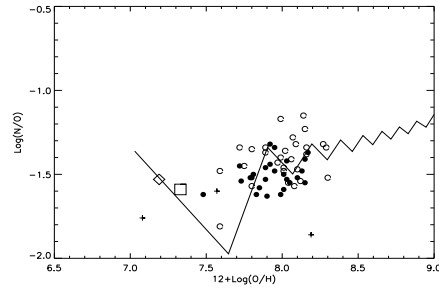


Figure 7. Same yield set and parameters as in fig 6, except that $m_L=0.01$, the mass of the first burst is $2 \times 10^6 M_\odot$ and the masses of the following bursts are $6 \times 10^6 M_\odot$. Compare the results to those of fig 6. It is evident that the observations are explained equally well using the low cutoff as when using the higher cutoff, if just burst masses are about twice as massive.

is well above the value obtained here. If α really is so large in AGB stars in the LMC, an explanation might be that the value of the convection parameter depends on metallicity, since the metallicity of the LMC is high (about half-solar). A higher value of α at high metallicities is not ruled out by the model as long as it is equal to 1.1 during the first few bursts.

A large spread is evident and sufficient to explain the observed scatter. Here, the plusses, representing the DLA-systems, are neglected. A similar run is presented in fig. 7, only employing the IMF having $m_L=0.01 M_\odot$. As expected, it is seen that the result resembles the situation in fig. 6, if one assumes all bursts to involve twice the mass of the bursts in fig. 6.

Figures 6 and 7 give a good comprehension of the outcome of the model, but some considerations should be made before any solid conclusions are drawn. Firstly, abundances are measured in H II-regions only, and therefore only at the 'positions' of the bursts, not in between. Secondly, the evolutionary path represents the evolution of one dwarf galaxy. Another dwarf galaxy, having different parameters such as total mass, burst masses etc., would have another evolution, and thus another path in the N/O-O/H plot. Thus, fig. 8 shows the evolutionary paths of dwarf galaxies having differ-

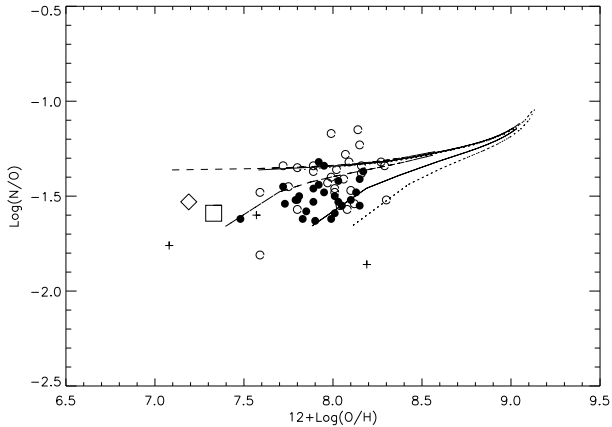


Figure 8. Three closed models, each with different burst masses, using set no. 2a. All other parameters are the same as in fig. 6. For each burst mass, two lines have been drawn: one through the upper points of the saw-tooth pattern and one through the lower points. The dashed lines correspond to burst masses equal to 1 per cent of the total mass of the galaxy, the solid lines to 3 per cent and the dotted lines to 5 per cent

ent fractional burst masses. Yield set 2a has been used, and all of the parameters, except the mass of each burst, are the same. To make the plot more clear, lines have been drawn through the first bursts of each pair, and through the second bursts. The former lines are almost coincident, because the time interval between two pairs of bursts is ~ 1 Gyr, enough to release almost all of the nitrogen. Thus, larger bursts increase both N and O, adjusting N/O to be roughly unchanged. The case is different for the lines through the second pair-bursts, because the N from the first pair-burst has not yet been released after 30 Myr. Thus, a larger burst mass gives an increase in O abundance only.

Two results may be deduced from fig. 8. Firstly, the scatter of the observations is perfectly explained, because an observational scatter of ~ 0.1 dex has to be taken into account. Furthermore, the area between the lower line corresponding to 5 per cent burst masses and the upper line is 'filled' in the sense that the distribution of burst masses may be everything between zero and 5 per cent to match the observations. Thus, the distribution of abundances is accounted for by using the models of dwarf galaxies having various reasonable relative burst masses. The other result is the slight increase of the evolutionary path toward higher metallicities. However, the small upturn may not be a consequence of dominating secondary N production, but rather the decreasing O yield at higher metallicities, see table 3.

Set no. 2b is different from no. 2a only in that a modest mass-loss from massive stars is assumed. The effect of this change on the evolutionary path is seen by comparing fig. 9 with fig. 8. It is possible directly to compare the model outputs of the two figures, since all parameters, including the burst masses, are identical. When using set 2b instead of 2a, the N/O ratio has an even smaller upturn at higher metallicities, because the O-yield is higher. Thus, even when N production is increasing at higher metallicities, so is the oxygen, keeping the ratio down and thereby hiding the secondary behavior of N. Still, the conclusions are the same:

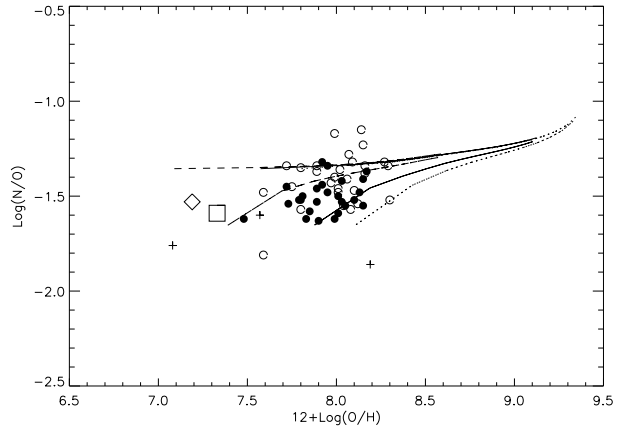


Figure 9. Evolutionary paths of three closed models using yield set 2b. The lines are drawn as in fig. 8 with identical parameters so the dashed lines correspond to burst masses equal to 1 per cent of the total mass of the galaxy, the solid lines to 3 per cent and the dotted lines to 5 per cent

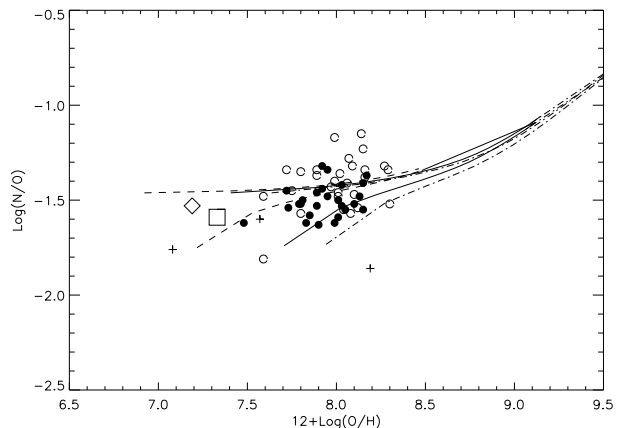


Figure 10. Three closed models each with different relative burst masses using the yields of set 3 (Padova). The meaning of the lines is the same as in fig. 8. The dashed line corresponds to burst masses equal to 1 per cent of the total mass of the dwarf galaxy, the solid line to 3 per cent and the dashed-dotted line to 5 per cent. It is worth noting that the mass interval for producing primary N is the same as in fig. 8. For these runs, all primary yields have been extrapolated for metallicities lower than the range covered by the yield sources.

both the level of N/O and the scatter is explained, independent of m_L .

Using yield set no. 3, the same kind of plot is constructed as those above. Here there is no explicit assumption on the convection parameter, but for reasons explained below, the primary component of N (and O) for $Z < 0.008$ has been extrapolated linearly, using the yields of $Z = 0.008$ and $Z = 0.02$ instead of just adopting the primary yield at $Z = 0.008$. The run of the model is presented in fig. 10. At least two features have to be mentioned. The first is that the scatter is somewhat smaller than for set 2a (or 2b) and the second is an upturn in N/O at higher metallicities, being more pronounced, than it was for set 2a and 2b. Unfortu-

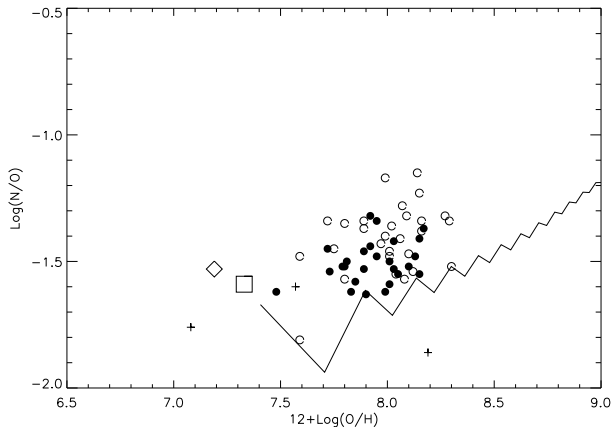


Figure 11. An evolutionary track, using set 3 yields. All burst masses are $3 \times 10^6 M_{\odot}$. The yields of primary components for metallicities lower than $Z=0.008$ are set equal to those given for $Z=0.008$.

nately, the upturn is taking place for higher oxygen abundances than those of the observations.

The primary component in set 3 has also been modelled in another way: For the same choice of parameters as in fig. 10 (solid line), the model has been applied with primary yields equal to the one at the lowest metallicity for which the yields are given ($Z=0.008$), with the resulting evolutionary path plotted in fig. 11. A comparison shows that an adoption of the primary yields at $Z=0.008$ will produce too little primary N. It seems to be necessary to make primary production more effective, the lower the metallicity, as it is done by the linear extrapolation, because the primary N yield at $Z=0.008$ is slightly larger than it is for solar metallicity. This is actually an important result, because it provides a constraint on the produced primary N, independent of stellar models. The explanation for this result might be that the number of thermal pulses in the AGB phase of low metallicity stars is higher, thus converting more C and O into N via the CNO-cycle. Hence, in the following, all model runs using set 3, will use linear extrapolations of primary N yields, below $Z=0.008$. Of course, one could make the IMF steeper thereby producing less oxygen. However, observations do not support a steeper IMF.

When comparing the outputs of the model, using set 2a (2b) and 3, it is important to remember that in set 2a and 2b, the lowest metallicity for which yields are available is $Z=0.004$, at least in the critical, and very important mass interval 4 to $5 M_{\odot}$, while it is as high as $Z=0.008$ in the same mass interval for set 3. Thus, whether primary N yields at $Z < 0.008$ are extrapolated from $Z=0.02$ over $Z=0.008$ or are adopted to be equal to the yield at $Z=0.008$, the result is quite uncertain, and stellar yields at much lower metallicities are definitely desirable.

5.1.2 Y - O/H

It is worth emphasizing that the helium abundances are fitted with input parameters not different from those used to fit the N/O ratio. For the closed model presented in fig. 8 by the solid line, Y has been calculated as well. Y against

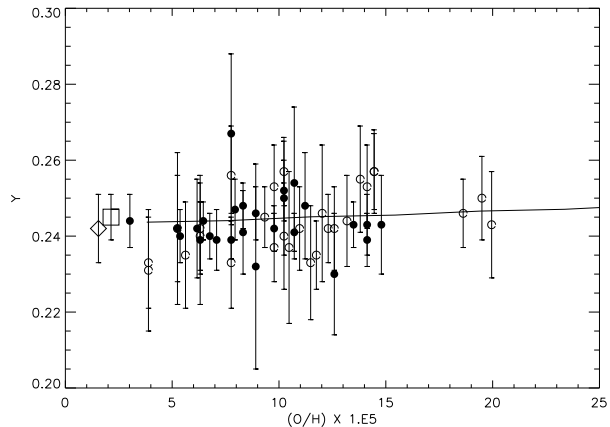


Figure 12. The evolution of the helium mass fraction Y as a function of O/H , using yield set no. 2a and $m_L=0.1$, plotted as a solid line. The model output of Y and O/H are from the same run as marked by the solid line in fig. 8, thus having a burst mass of 3 per cent of the total galaxy mass. The meaning and sources of the symbols are the same as in the N/O - O/H plots, except that the DLA systems are not represented. Note that the O/H axis is not logarithmic.

O/H is shown in fig. 12. The evolutionary Y path does not show any scatter, though the dwarf galaxy is double bursting, because about half of the helium is produced in massive stars, together with the oxygen. The fit is very good and well within the error bars. For the two most metal deficient objects in the plot, IZw18 and SBS0335-052, it seems to be necessary to assume smaller burst masses, say 1 per cent of the total mass - the model with the dashed lines in fig. 8. Thus, these objects can be explained by experiencing their second burst and having burst masses equal to 1 per cent of their total mass. The output of the model gives the abundances just before every burst. Hence, to calculate the model value of dY/dZ , the $Y, O/H$ values were fitted using a linear least-square fit, assuming $Z=20(O/H)$. The result is 1.0, lower than the (very uncertain) value of 2.6 derived from the observations, see section 2. The corresponding result using set 2b is not shown, since it resembles the one by set 2a. Certainly, it is true that the He yield is smaller for modest mass loss, but only for very massive stars and high metallicities (Maeder 1992).

The dependency of He on O is more pronounced, when using the Padova yields, as seen in fig. 13. Calculating dY/dZ , using this yield set, in the same way as done for set 2a one obtains 3.1, higher than the value calculated for the observations (2.6). From table 3 it is clear that the true He yields for set 3 are a factor of ~ 3 higher than those of sets 2a and 2b, but it is unclear why the Padova tracks produce that much helium. This feature makes the fit not quite as good as it was for set 2a (2b). However, the primordial helium determination is only certain within 0.003 (Izotov et al. 1997a). Setting the primordial He abundance equal to the lower limit (0.240) in the initial conditions of the model does not change the N/O- O/H evolutionary path, but it does lower the level of Y in fig. 13. The new evolutionary path of Y has the same slope as the solid one of course, but sufficiently lower to be a fairly good fit, as it appears well within the observational uncertainties.

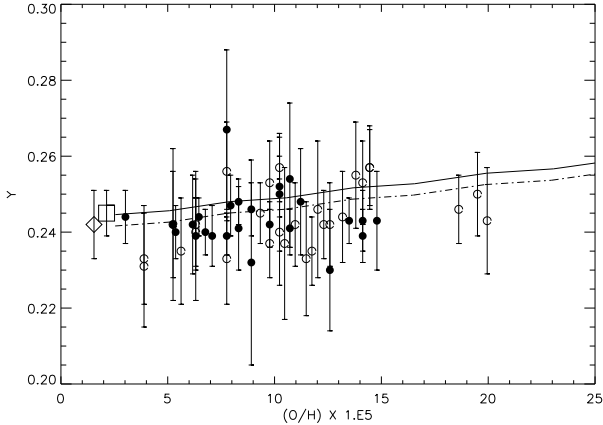


Figure 13. The evolution of Y using the Padova yields. The solid line is the evolutionary path, using a primordial He abundance $Y_p=0.243$, from the same model run as used for the solid line in fig. 10, and the dashed-dotted line is the corresponding path, assuming $Y_p=0.240$, still within the uncertainties of the primordial He determination. The mass of each burst is 3 per cent of the total mass in both cases.

5.1.3 $O/H - \mu$

Gas fractions may be useful in serving as a further constraint on chemical evolution models. It has been pointed out by several authors that closed models, such as the one presented above, are unable to explain the observed gas fractions (Matteucci & Chiosi 1983; Matteucci & Tosi 1985; Carigi et al. 1995). Thus, gas fractions have been calculated just before every burst using eqs. 23 and 24 allowing for comparison with some observed values from the literature.

Problem lies in the interpretation of the observations. The total dynamical mass of a dwarf galaxy also includes dark matter (DM). This dark is unlike to participate in the chemical evolution. Our model is including baryonic matter only. Thus, in order to compare the observations with the calculated gas fractions, one has to be sure that no significant amount of non-baryonic DM is included in the total mass estimates. However, as pointed out by several authors (Brinks & Klein 1988; Kumai & Tosa 1992; Carigi et al. 1999; Meurer 1998) dwarf galaxies, including BCGs, are DM-dominated. Consequently, dynamical estimates of total masses are useless, when considering dwarf galaxies. Carigi et al. (1999) tried to solve the problem by using dynamical estimates within the visible Holmberg radius, to avoid inclusion of a DM halo. Unfortunately, this leaves us with a very small sample of observations, and still the amount of DM within the Holmberg radius is uncertain.

However, gas fractions are one of the few possible ways of constraining chemical evolution models, so a discussion of gas fractions, using the same models as in the preceding paragraphs should be included. To avoid erroneous conclusions, we used lower and upper limits of the gas fractions.

The gas fractions used are presented in table 5. The gas masses included are HI-masses multiplied by 1.3 to account for the helium content. The amount of H_2 is ignored. All dynamically estimated gas fractions have been scaled to a Hubble constant $H_0 = 65 \text{ km s}^{-1} \text{ Mpc}^{-1}$ using

$M_{gas} \propto (\text{distance})^2$ and $M_{tot} \propto (\text{distance})$, so the gas fraction $\mu \propto (\text{distance}) \propto H_0^{-1}$.

DM is implicitly included, and molecular hydrogen is ignored, hence these gas fractions must be regarded as lower limits. Unfortunately, even the lower limits seem to be very uncertain. For instance, the gas fraction of IZw18 was first calculated using the data from Staveley-Smith, Davies & Kinman (1992). However, after He-correction and H_0 -scaling, the gas fraction became larger than 1. This is also the case for some of the galaxies in the Thuan & Martin (1981) sample (not included in the present sample). In the case of IZw18, the value 15 per cent gas has been adopted from Matteucci & Chiosi (1983). Extreme upper limits have been obtained assuming that each of the galaxies are experiencing their first burst, and are observed during maximum luminosity. Indeed, this is an extreme upper limit, and should be regarded as such. Adopting the evolutionary stellar models of Leitherer & Heckman (1995), the M/L_B ratio may be estimated for a burst, M being the mass of stars. Leitherer & Heckman calculated the blue luminosity for a $10^6 M_\odot$ starburst as a function of time. To be consistent, their Salpeter IMF has been scaled to ours. Indeed, two different IMF's have been used so far, but to be sure that upper gas fraction limits are obtained, the high lower limit, $m_L=0.1 M_\odot$, is used, as this gives the lowest M/L_B , hence the highest gas fraction. The scaling is very simple, since the only difference is to scale the lower mass limit from 1 to $0.1 M_\odot$. Hence, all luminosities from Leitherer & Heckman are multiplied by 0.39. From their fig. 9 ($Z=0.1 Z_\odot$), the minimum magnitude is read off to be -16.4 corresponding to a maximum luminosity $\sim 5.6 \times 10^8 L_\odot$ using the absolute blue solar magnitude 5.48. After IMF scaling this gives $\sim 2.2 \times 10^8 L_\odot$, so $M/L_B \sim 0.004$. In table 5 the observed blue luminosity, scaled to $h=0.65$, is given for each galaxy. Table 5 gives the corresponding gas fraction, as $\mu = M_{gas}/(M_{gas} + M_{stars})$. If IZw18 is experiencing its first burst, this upper limit should be realistic as its true gas fraction. The large difference from the dynamically derived gas fraction is caused by a combination of influence from DM, poor total dynamical mass estimation or/and that IZw18 is not experiencing its first burst.

To constrain the models more, three more galaxies have been included, for which we know that they are definitely not experiencing their first burst. One of them is the LMC. Strictly speaking, the LMC is not a dwarf galaxy, but in many ways it behaves as such. For these three galaxies, M/L_B is assumed to be 0.5, not as extreme as above, thus obtaining upper limit gas fractions lower than for the other galaxies. Does this assumption still provide an upper limit for the gas fractions? The answer is confirmatory, if the assumed M/L_B is a lower limit. The ratio is estimated using the star formation histories of LMC (Geha et al. 1998, fig.7(c)), SMC (Pagel & Tautvaišienė 1998), and NGC6822 (Gallart et al. 1996, fig.12). The general procedure is quite simple. First we find L_B of the objects by using a stellar population synthesis model and the SFH. The blue magnitudes in Charlot & Bruzual (1991, fig.5, dashed line) are calibrated by using Leitherer & Heckman (1995, fig.10, 0.25 Z_\odot , solid line). When we know the age of a starformation epoch, we may find the blue magnitude, hence the luminosity by reading off figure 5 of Charlot & Bruzual. The results are valid for $m_L=1 M_\odot$, $m_U=100 M_\odot$ and a starformation rate

Table 5. The data used for gas fraction plots.

Name	L_B (L_\odot)	M_{gas} ($10^8 M_\odot$)	$\log\left(\frac{M_{gas}}{M_{tot}}\right)$	$\log\mu$	$12 + \log(O/H)$
	(1)	(2)	(3)	(4)	(5)
Mrk 5	0.35E+9	2.25	-2.65E-3	-0.13	8.21
36	0.96E+8	0.33	-5.03E-3	-1.19	7.85
67	0.17E+9	0.28	-1.07E-2	-0.52	8.21
178	0.96E+8	0.24	-6.82E-3	-0.09	7.95
71	0.11E+10	17.1	-1.16E-3	-0.01	7.89
209	0.76E+8	0.87	-1.52E-3	-0.38	7.81
600	0.44E+9	5.71	-1.34E-3	-0.68	8.01
IZw18	0.10E+9	1.12	-1.63E-3	-0.83	7.22
IIZw40	0.23E+9	7.79	-5.04E-4	-0.29	8.14
IIZw70	0.15E+10	5.88	-4.31E-3	-0.54	8.06
VIIZw403	0.53E+8	0.66	-1.40E-3	-0.39	7.73
IZw49	0.17E+10	7.96	-3.76E-3	-0.28	8.03
IZw123	0.36E+9	0.85	-7.31E-3	?	8.10
CG 1116+51	0.15E+9	3.63	-7.00E-4	-0.07	7.52
SBS 335-52	0.98E+9 ^e	1.94 ^e	-8.80E-3	?	7.33
NGC 6822	0.18E+9 ^a	2.53 ^a	-0.13 ^d	-0.80	8.19
SMC	0.99E+9 ^b	4.66 ^c	-0.31 ^d	-0.38 ^a	8.04
LMC	0.47E+10 ^b	6.90 ^c	-0.65 ^d	-0.92 ^a	8.36

(1) The blue luminosities are from Thuan & Martin (1981) with four exceptions, see (a,b,e). The luminosities are scaled to $h=0.65$. (2) The gas masses are from Thuan & Martin, though see (a,c,e). All values are scaled to $h=0.65$. (3) The logarithm of the calculated upper limit gas fractions, where $M_{tot} = M_{gas} + M_{stars}$. M_{stars} has been calculated assuming the galaxies to do their very first burst, see text and note (d). (4) The logarithm of the observed, lower limit gas fraction. μ is the gas mass divided by the dynamically estimated total mass from Thuan & Martin (1981), Matteucci & Chiosi (1983) and Taylor et al. (1994). The question marks indicate that the gas fraction is not found, so in these cases, only the upper limits are used. All values are scaled to $h=0.65$, though see note (a). (5) The oxygen abundances from Kobulnicky & Skillman (1996), Pagel et al. (1992) and Izotov et al. (1997a).

(a) Values are from Lequeux et al. (1979), obtained by h -independent distance measurements. Hence, these values are adopted without any scaling.

(b) These luminosities are calculated from the absolute magnitudes given in Matteucci & Tosi (1985), using the solar absolute blue magnitude 5.48.

(c) Values from Carigi et al. (1999). They give the gas masses directly for $h=0.65$ and account for H_2 . To be consistent with the rest of our sample, their values are divided with 1.1 to obtain gas masses not including molecular hydrogen.

(d) These galaxies are known for sure not to experience maximum luminosity of their first starburst at the present epoch. Thus, more realistic upper gas fraction limits have been calculated, assuming their M/L_B ratio to be 0.5, see text for further details.

(e) Values from Thuan, Izotov & Lipovetsky (1996)

of $1M_\odot yr^{-1}$, since the magnitudes are calibrated by using Leitherer & Heckman. By doing this we ignore the very few stars with masses between $100M_\odot$ and $125M_\odot$ originally included by Charlot & Bruzual. This will not have any significant effect on the results.

For LMC we have the SFR in relative units. We have splitted the SFH into two star formation epochs, one that started 2 Gyr ago and one 12 Gyr ago. Integration of the SFR and weighting the two read-off luminosities with respect to SFR leads to $M/L_B=0.4$. By scaling the luminosities to $m_L=0.1M_\odot$ and $m_L=0.01M_\odot$, we obtain $M/L_B=1.0$ and 2.4, respectively.

For NGC 6822 we are given the SFR in absolute units, but we restrict ourselves to use the relative SFR only. Again we split the SFH into two epochs. A very recent one that started 200 Myr ago and a very old one that started 15 Gyr ago. As we ignore the epoch that stopped 5 Gyr ago, we will obtain a lower estimate of M/L_B . Using the method

outlined above, we get $M/L_B=0.16$, and 0.42, 0.96 for the 0.1 and 0.01 lower mass limits, respectively.

The lack of knowledge of the SFH in the SMC is remarkable. Hence, we have used the SFH from the model by Pagel & Tautvaisene (1998), which has succes in explaining e.g. $[Fe/H]$. The SFR is given in absolute units in their table 2, so integration yields the total mass of stars. Using $L_B = 0.99 \times 10^9 M_\odot$ from table 5, we arrive at $M/L_B=0.43$.

In conclusion we have that $M/L_B=0.5$ is a conservative lower limit, hence giving an upper limit on the gas fraction.

The results from the calculations are shown for yield set 2a (top plots) and 3 (bottom plots) in fig. 14. In both cases, using the IMF with $m_L = 0.1 M_\odot$, the fits are always between the lower and upper limits, except for the three 'moderate upper limit' galaxies. Lowering the yield by adopting $m_L = 0.01 M_\odot$, helps somewhat, but only one of the three moderate galaxies is fitted, namely NGC 6822, the two others being out of range.

Since the model fails in explaining the more restrictively

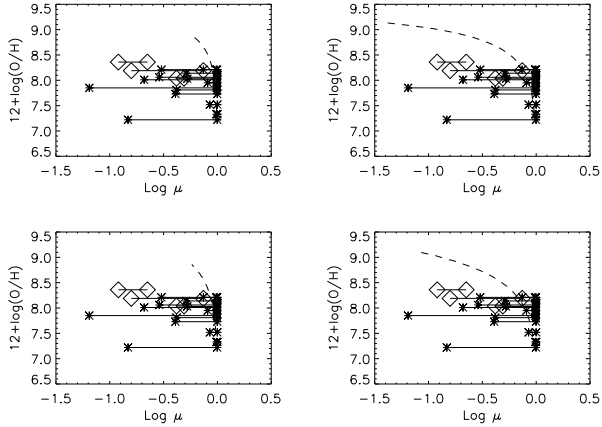


Figure 14. $12 + \log(\text{O}/\text{H})$ as a function of gas fraction, $\mu \equiv \frac{M_{\text{gas}}}{M_{\text{gas}} + M_{\text{stars}}}$. Top plots are for set 2a, for $m_L = 0.1 M_\odot$ to the left and $m_L = 0.01 M_\odot$ to the right. Bottom plots are for set 3, again $m_L = 0.1 M_\odot$ to the left and $M_{\text{low}} = 0.01 M_\odot$ to the right. The dashed lines are the results of our closed models, using burst masses equal to $2 \times 10^6 M_\odot$ for the plots on the left and $4 \times 10^6 M_\odot$ for the plots on the right. The stars are the lower and upper limit gas fractions for the majority of the sample, connected by lines. The diamonds are the limits given for the three galaxies, having more moderate upper limits.

chosen galaxies, the yields have to be lowered further. The number of low-mass stars could be increased, but it would be parameter-gambling, not appealing very much to a physical control of the model. However, it should be noted that Carigi et al. (1999) use this possibility to solve the problem. Keeping the IMF, the only way of lowering the yield is to open the model and allow for galactic winds, ordinary or enriched (Carigi et al. 1995) or/and inflow (Pagel & Tautvaišėnė 1998).

5.2 The model including enriched winds

From this place forth, the model is opened, allowing for gas exchanges with the intergalactic medium. All simulations have used $m_L = 0.01 M_\odot$.

The results of including enriched winds are shown in fig. 15 for set 2a and fig. 16 for set 3. As seen, the wind efficiencies employed are the lowest acceptable for fitting the gas fractions of the Magellanic clouds. Using the same model, the outputs have been plotted with the observations for both N/O-O/H and Y-O/H.

However, removing that much oxygen raises the N/O ratio high above the level of the observations. One could try to reduce N/O by lowering the value of α , in the case of set 2a, but a value much lower than 1, seems to be quite unrealistic, seen in the light of recent work on stellar evolution, e.g. Marigo (1998).

For set 3 (fig. 16), it is clearly seen that setting the primordial He fraction equal to its lower uncertainty value, as done when using set 3 in the closed model (see fig. 13), is not capable of explaining the He fractions, when introducing these high-efficient enriched winds - the fits are much too poor.

Hence, introducing enriched winds makes it impossible

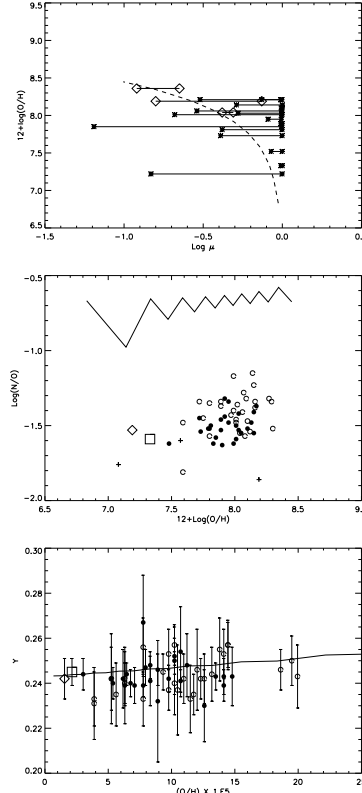


Figure 15. The results of models with enriched winds. The plots are made, using an efficiency factor equal to 0.8, adequately to fit the gas fractions. The yield set in use is 2a. The values of M_{HBB} and α are the same as used for the closed models, thus being $5 M_\odot$ and 1.1, respectively. All burst masses are equal to $6 \times 10^6 M_\odot$.

to fit gas fractions and N/O simultaneously. Further, in the case of set 3, problems also arise in fitting the He fractions.

5.3 The model including ordinary winds

Though keeping the mass of each burst as a free parameter, it turns out that $2 \times 10^6 M_\odot$ is fulfilling the requirement on placing the second burst close to the abundances of IZw18. Thus, it is appropriate to keep this burst mass constant in the following discussion. The results are shown, in fig. 17 for set 2a and fig. 18 for set 3.

It was shown above that the scatter in N/O could be explained by our model. Hence, the scatter will not be given much attention in the following, as the work will be concentrated on getting the right level of N/O, coincident with the gas fraction fitting, if possible.

From the top plots, it is evident that a mass removal of 5 times the burst mass does not appreciably change the appearance of the fits from the closed model. Actually, the O-yield is lowered only by ~ 0.3 dex as seen when comparing to fig. 14, using 2a yields. The point may be that we are dealing with a discontinuous star formation. Note for instance the upper linear part of the model curve. The increase in O/H along this part is due to one burst only, as seen when comparing to the corresponding N/O plots. The explanation is that the smaller the absolute gas mass, the larger the ef-

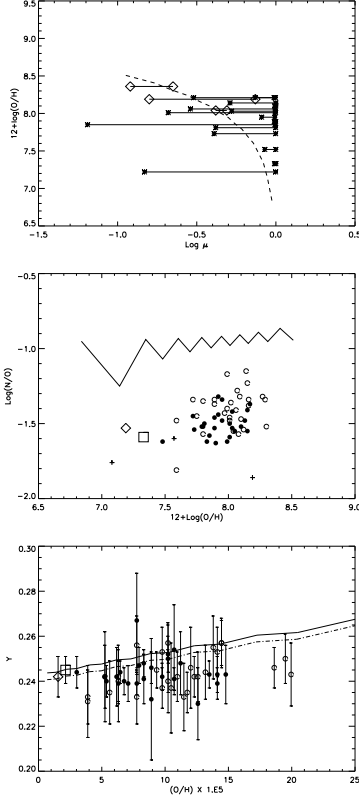


Figure 16. The results using the same parameters as in fig. 15, but with yield set no. 3 (Padova yields). The efficiency factor is 0.7, chosen to fit the gas fractions.

fect of oxygen enrichment. Thus, even when adopting higher wind efficiencies, it is not possible to bring the oxygen yield sufficiently down. The same mechanism is responsible for increasing the scatter in N/O for higher wind efficiencies. Hence, it is possible to produce large scatter without having a large burst mass.

Note also that the evolutionary tracks stay close to a gas fraction of 1 for a relatively large part of the evolution. A simple calculation will show, how difficult it is to bring the gas fraction down. For instance, assume the first burst to turn $2 \times 10^6 M_{\odot}$ into stars, and set $W_{ISM} = 5$. Then, just before the second burst, the gas fraction will be

$$\mu \equiv \frac{M_{gas}}{M_{tot}} = \frac{M_{gas}(0) - 2 \times 10^6 M_{\odot} - 10^7 M_{\odot}}{M_{tot}(0) - 10^7 M_{\odot}} \quad (30)$$

$$= 0.98,$$

since the initial mass of the dwarf galaxy is $M_{gas}(0) = M_{tot}(0) = 10^8 M_{\odot}$. Using the equation again, one finds $\mu = 0.95$ just before the third burst. These values are lower limits (!), since the increase in gas from stellar ejecta is disregarded.

Both the level of N/O and slope of Y are satisfied. Note the similarity between the Y plots presented here and those presented by the closed model. This is not surprising, as about half of the helium is produced by massive stars, hence following oxygen. Status is that all observations are matched reasonably well by including ordinary winds, but no better than for the closed model. In particular, it is found that it

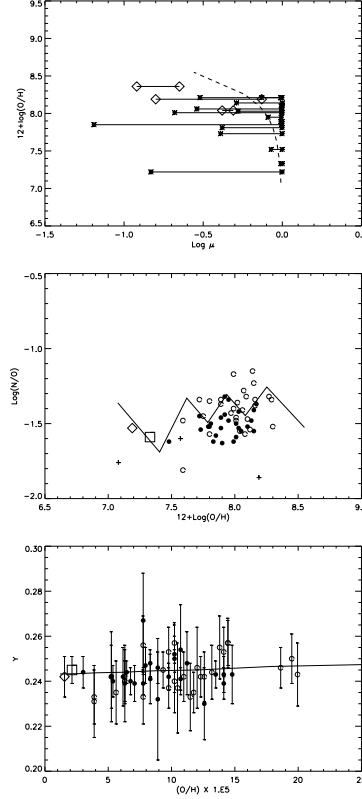


Figure 17. The results of using a model including ordinary winds. The plots are made using $W_{ISM} = 5$. Note the increasing scatter in N/O as a function of W_{ISM} explained in the text. The yield set in use is 2a. The values of M_{HBB} and α are still $5 M_{\odot}$ and 1.1, respectively, and the mass of each burst is $2 \times 10^6 M_{\odot}$.

is impossible to bring the yields sufficiently down to explain the gas fraction intervals of the Magellanic clouds.

5.4 Comparing the ordinary wind model with an analytical model

A few calculations have been performed, using a simple analytical model, employing continuous star formation and Hartwick-outflow. The outputs of the analytical model and the numerical model are then compared. The comparison is only performed for yield set 2a, since the inclusion of winds is identical using set no. 3.

The general formulation of Hartwick-outflow is

$$\frac{dM_{dw}}{dt} = -W_{ISM} \frac{dM_s}{dt} \quad (31)$$

where M_{dw} is the mass of the dwarf galaxy and M_s is the mass of stars. The next step is to use

$$\frac{dZ}{dM_s} = \frac{p}{M_g} \quad (32)$$

obtained by considering the changes in Z as a result of stellar ejecta, star formation and outflow, see e.g. Pagel (1997, his eq. 7.37). Instantaneous recycling is assumed, and so is the absence of inflow. Separating the variables and using $\delta M_g = -\delta M_s - W_{ISM} \delta M_s$, one finds

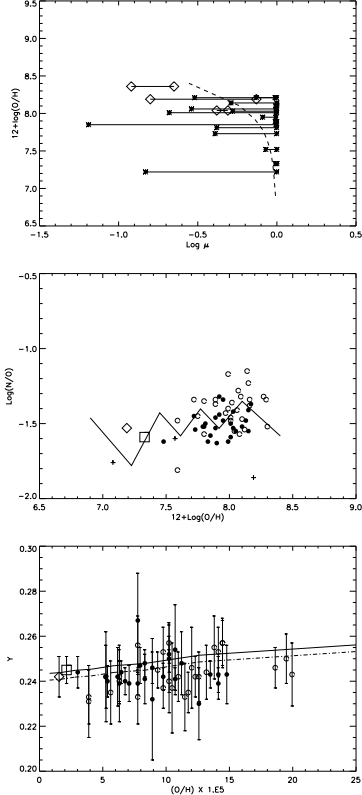


Figure 18. The results using the same wind and mass parameters as in fig. 17, but with yield set no. 3.

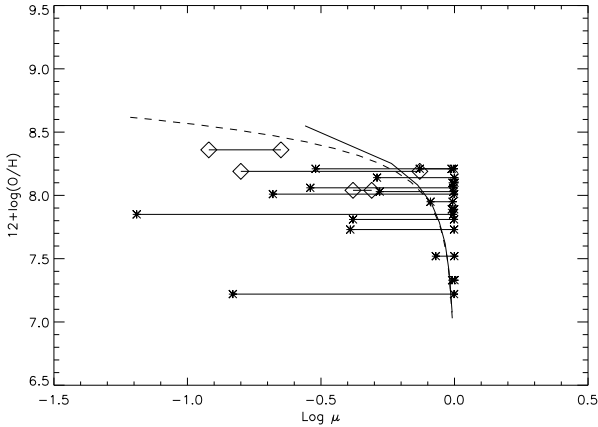


Figure 19. The comparison between the numerical bursting model employing ordinary winds with $W_{ISM}=5$ and burst masses $2 \times 10^6 M_{\odot}$, and the continuous star forming analytical model. The solid line is the numerical bursting model.

$$\frac{Z}{p} = \frac{1}{1 + W_{ISM}} \ln \left(\frac{M_g(Z=0)}{M_g} \right) \quad (33)$$

where the yield is assumed constant. The total mass of the dwarf galaxy is written

$$M_{dw} = M_{dw}(Z=0) - W_{ISM}M_s \quad (34)$$

$$= M_g(Z=0) - W_{ISM}(M_{dw} - M_g) \quad (35)$$

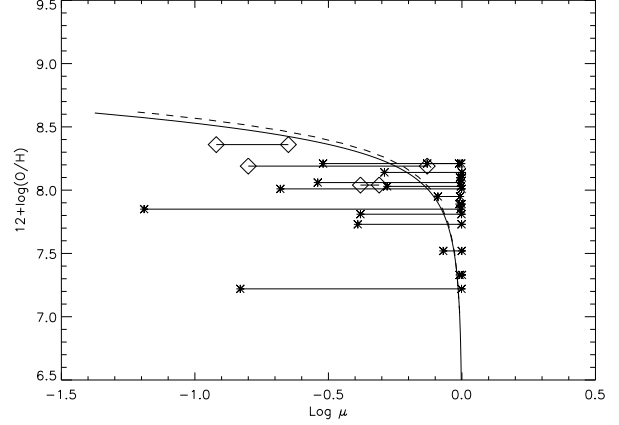


Figure 20. Comparing the analytical model from fig. 19 with the semi-continuous numerical model. The solid line is the numerical model and the dashed line is the analytical model. See text for details.

Isolating $M_g(Z=0)$ and inserting it into eq. 33 gives

$$\begin{aligned} \mu &= \frac{1 + W_{ISM}}{\exp\left(\frac{Z}{p}(1 + W_{ISM})\right) + W_{ISM}} \quad (36) \\ &= \exp\left(-\frac{Z}{p}\right) \frac{1 + W_{ISM}}{\exp\left(W_{ISM}\frac{Z}{p}\right) + W_{ISM} \exp\left(-\frac{Z}{p}\right)} \end{aligned}$$

where μ is the gas fraction $\frac{M_g}{M_{dw}}$. It is seen that for a closed model, $\mu = \exp\left(-\frac{Z}{p}\right)$. For our numerical model, the yield is metallicity-dependent. Hence, $\exp\left(-\frac{Z}{p}\right)$, equal to the gas fraction at Z for a characteristic value of p , is found from the closed numerical model. Inserting this into eq. 36, finally gives the gas fraction of the analytical model, now employing metallicity-dependent yields and outflow.

The results are shown in fig. 19 for $W_{ISM}=5$. The numerical fit (solid line) is the same as in fig. 17. Note that for a large part of the evolution, the two models are coincident, but at the last part they are differing from each other. It is likely that the difference is a result of using instantaneous bursts instead of a continuous SFR. The point may be that the mass of gas is small at the last part of the evolution. Thus, the relative amount of ejected oxygen from one burst, is high compared to the gas mass, hence giving a large increase in O/H.

To make a further check on this hypothesis, a continuous version of the numerical model has been made. This is done in an approximate way, introducing the following changes to the above numerical outflow model:

(i) The bursts are all single bursts, i.e. all interburst periods are the same.

(ii) The interburst periods are made short. The shorter the interburst period, the more continuous the star formation. An interburst period of 3 Myr was sufficient for our purpose.

(iii) The masses of the bursts are calculated by assuming a mean SFR. The calculations here assume $\langle \text{SFR} \rangle = 0.002 M_{\odot} \text{ yr}^{-1}$, corresponding to one burst of mass $2 \times 10^6 M_{\odot}$ every Gyr. A reasonable value compared to the calculations

above. The masses of the bursts are then equal to $0.002 M_{\odot} \text{ yr}^{-1} \cdot 3 \text{ Myr} = 6000 M_{\odot}$.

All other calculations are performed exactly the same way, as they were, using the double bursting model. The calculations are performed for $W_{ISM}=5$ and compared to the analytical model from fig. 19. From fig. 20, it is seen that the two models are almost identical. The small offset may be caused by the calculation of the analytical model, adopting the yields from the closed numerical bursting model. The similarity between the two models confirms the suspicion that instantaneous bursting models behave differently from continuous models, as the numerical model is the same that produced the fit in fig. 19, except for the semi-continuous star formation.

5.5 The model including ordinary winds and inflow

The introduction of inflow gives two new parameters: the total mass accreted onto the galaxy M_0 and the duration of the inflow event τ_{inf} . Only results for a few parameter choices are shown and interpreted by close examination of the results.

The gas fractions of the three selected galaxies provide strong restrictions on the possible parameter space, since inflow and outflow balance each other for obtaining the right gas fraction values. Hence, if one increases the rate of inflow, one has to increase the rate of outflow as well. Otherwise, the modelled gas fractions would be too high, and the three selected gas fraction intervals would never be reached.

It is assumed that the mass of the original gas cloud is 0 at $t=0$. However, inflow of gas increases the mass of the gas cloud, until it starts to form stars at a mass threshold $M(t')$. The time t' is calculated using eq. 20, giving

$$t' = \tau_{inf} \ln \left(\frac{M_0}{M_0 - M(t')} \right) \quad (37)$$

For consistency with previous calculations, the threshold is assumed to be $10^8 M_{\odot}$. Thus, after a time t' , the first burst appears. As for all the previous models, the first burst is a single one, and all other bursts appear in pairs. Hence, the appearance of the first burst is delayed by the time t' , when comparing to the models not including inflow. This time difference is included, when calculating the age of the system. Remember that the model terminates if the system is older than 15 Gyr.

For yield set 2a, the results are displayed in figs. 21, 22 and figs. 23, 24.

For the parameter values chosen very small scatter results in the N/O diagram in fig. 21. The plots were made using a high inflow/outflow rate to lower the yield sufficiently to fit the gas fractions of NGC 6822 and the Magellanic clouds. The price to pay seems to be a very small scatter in N/O. Hence, in fig. 22 a low rate of inflow has been assumed, in particular at late stages of evolution, as τ_{inf} is decreased to 2 Gyr. Now, it is possible to explain the scatter in N/O, but the result is an unsatisfactory gas fraction fit. Obviously, a large inflow rate of primordial gas buffers the impact of O-rich ejecta on the ISM abundances, resulting in small scatter.

To investigate further, whether it is possible or not to

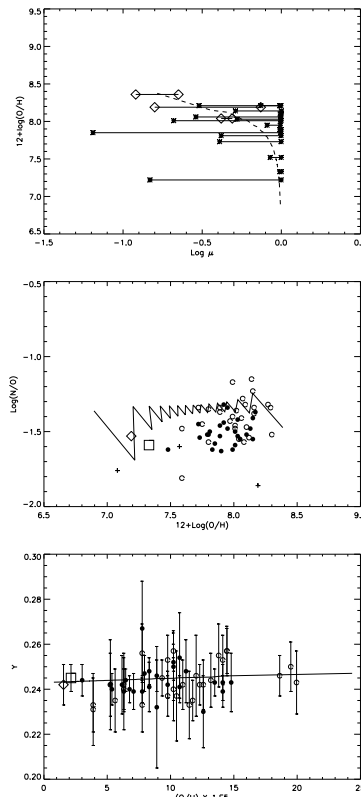


Figure 21. The results of including both inflow and ordinary winds. Here the yield set used is no. 2a. The plots show a run using $\tau_{inf}=5$ Gyr and $M_0 = 8 \times 10^8 M_{\odot}$. The burst masses are $3 \times 10^6 M_{\odot}$, and $W_{ISM}=8$.

explain the scatter in the N/O-O/H diagram and gas fractions simultaneously, the outflow parameter is kept at 8, but the burst masses are increased to $8 \times 10^6 M_{\odot}$ to give a larger scatter. To balance the high outflow rate (remember that the outflow rate is proportional to the burst mass) a rather high inflow rate is needed, $(\tau_{inf}, M_0)=(5 \text{ Gyr}, 10^9 M_{\odot})$.

The results are shown in figs. 23 and 24. Note that the high outflow/inflow rate forces N/O to increase dramatically with increasing O/H, because inflow of primordial gas decreases O/H, but not N/O. At the same time, the strong outflow decreases the O abundance more than the N abundance, since the composition of the ISM just before each second pair-burst is O enhanced, hence giving an O enhanced wind (though defined and treated as an ordinary wind).

The corresponding gas fraction plot fits NGC 6822 and SMC, but the LMC gas fraction and abundance are never reached. Note the 'sawtooth' behavior in the gas fraction plot. During the long interburst period, the high inflow rate deposits a large amount of H in the ISM, but no O, hence decreasing O/H until the next burst enriches the ISM again. However, the gas fraction does not increase, because the inflow is balanced by the high outflow rate. From these last results, it seems to be possible to explain both the scatter in N/O and the gas fractions simultaneously, but note that in our struggle to explain the gas fractions of the three selected galaxies, some 3-4 other dwarf galaxies are not fitted within the intervals. Note also that the closed model explained those gas fractions quite well!

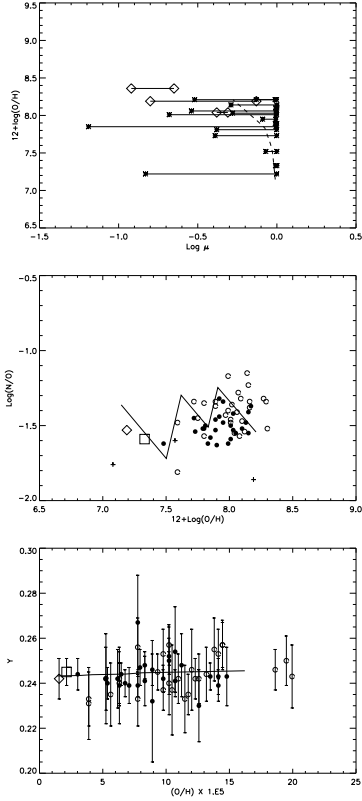


Figure 22. Still using set 2a, though trying to increase the degree of scatter. Now, the two parameters of inflow are $\tau_{inf} = 2$ Gyr and $M_0 = 2 \times 10^8 M_\odot$. The burst masses and wind parameter have the same values as in fig. 21.

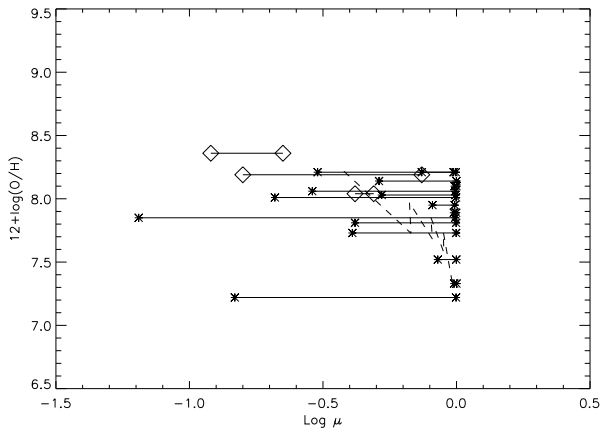


Figure 23. Another model using yield set 2a, employing burst masses equal to $8 \times 10^6 M_\odot$, $M_0 = 10^9 M_\odot$, $\tau_{inf} = 5$ Gyr and $W_{ISM} = 8$. Note the 'sawtooth' behavior caused by the high inflow rate.

The results using yield set 3 are displayed in fig. 25. The gas fractions of the three well-known galaxies are properly fitted, though the same remark as above has to be made, namely that the fits are outside the intervals of 3-5 other dwarf galaxies.

The right level of N/O is obtained. Note in particular

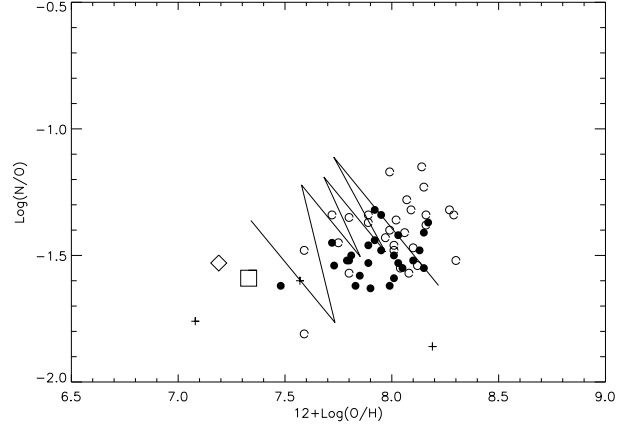


Figure 24. The evolution of N/O-O/H for the same model as in fig. 23.

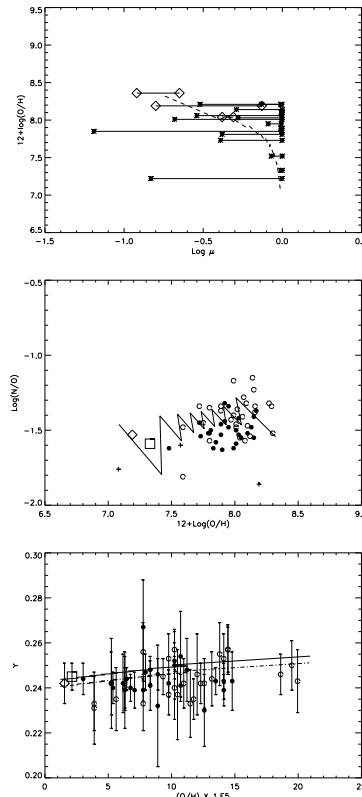


Figure 25. Results using yield set 3. For the model represented here the adopted burst masses are $6 \times 10^6 M_\odot$ and $M_0 = 7 \times 10^8 M_\odot$. Finally, $W_{ISM} = 5$ and $\tau_{inf} = 5$ Gyr.

the increasing N/O in the left plot, following the trend of the observations. As for set 2a the scatter in N/O is rather small, and insufficient to explain the observed scatter.

The four Y-O/H plots have not yet been discussed, but it may be done in a few words. The model predictions match the observations quite well, but they are of course still showing the difference in slope between set 2a (or 2b) and 3.

6 DISCUSSION

Numerical models calculating the chemical evolution of gas-rich dwarf galaxies have been presented. The models have been fitted to a sample of abundance and gas fraction observations. A chemical evolutionary model has to fit these observations simultaneously. It is clear that a realistic model is not just a couple of equations including a lot of parameters that one can change until all data are fitted. One has to remember that the equations are applied to a physical system, obeying physical laws. Hence, before doing any calculations, some considerations were made about ejecta dispersal and mixing processes. It was found that the processes involved are complicated and no complete theory exists yet. However, the four most important features in the enrichment process are found to be stellar ejecta, giant H II-regions, wind-driven superbubbles and SN-driven supershells. Wind-driven superbubbles arise shortly after a burst due to the strong stellar winds of massive stars. The radii of these superbubbles are in general smaller than the radii of the H II-regions. As the massive stars explode as SNe, a supershell is swept-up, soon catching up on the superbubble. However, a simple calculation showed that their radii become comparable to the radii of H II-regions only in the late stages of H II-region existence. Hence, it is suggested that observed emission lines, used for abundance determinations, arise in the ionized medium outside of the superbubble/supershell. Numerical hydrodynamical models indicate that SN-ejecta always stay within the supershell. If this is true, the observed abundances are not affected by the SN-ejecta from the stars producing the H II-region, hence being typical for the ISM.

The details of supershell evolution are still not known, but both theory and observations support star formation in expanding shells. From theory, it is expected to start not earlier than about 20 Myr after the starburst, resulting in star formation involving a mass comparable to the mass of the burst that initiated the supershell, hence appearing as a double burst. The double bursting mode of our numerical model ensures the appearance of scatter in the N/O-O/H plane, according to the time-delay idea, namely that N is released some time after O. The time interval between the two bursts of a pair is tuned to give maximum scatter. It is found that this timescale is comparable to the timescale of star formation in an expanding supershell. The requirement for the 'shell burst' to be the second pair-burst is that the O-rich ejecta mix into the supershell. Because of the poorly understood physics of supershells and mixing processes, this assumption should be seen so far as a working hypothesis. All bursts are assumed to be instantaneous, hence representing short but intense star formation events. The closed model is able to explain the observations of N/O-O/H in both scatter and level. If assuming the upper limit of hot bottom burning to be $5M_{\odot}$, $\alpha=1.1$ is used to explain the observations, where α is the mixing length parameter. This is a rather low value compared to the results of recent works however (van den Hoek & Groenewegen 1997; Marigo et al. 1998), favouring a value close to 2.

Using yield set 3 (the Padova set), it is necessary to extrapolate the primary N yields below $Z=0.008$ to obtain a higher N yield. Otherwise, the level of N/O becomes too low compared to the observations. The primary N production has to be increasing with decreasing metallicity. Calculations of stellar yields for metallicities lower than $Z=0.008$ are definitely desired to quantify this.

lations of stellar yields for metallicities lower than $Z=0.008$ are definitely desired to quantify this.

A very important conclusion is that no primary N production in massive stars is needed to explain the observations. Intermediate mass stars are in position to produce a sufficient amount of primary N.

For the Y-O/H observations, a linear trend is visible, and a linear fit gives $dY/dZ = 2.63 \pm 2.21$ and $Y_p = 0.238 \pm 0.004$. These values are consistent with those of Izotov et al. (1997a) within the uncertainties. The closed model is found to explain the Y-O/H observations perfectly, only with different slopes, depending on the yield set in use. In all cases the slopes are within the uncertainties. As seen by inspection of the true He yields for the three sets in table 3, one finds the explanation for the slope difference to be that the He yields of set 3 are 2-3 times higher than those of set 2a or 2b.

It is noteworthy that the Y-O/H relation was fitted using exactly the same parameters as for the N/O-O/H fitting. The problem arises when fitting O/H- μ data. It is argued that the observed gas fractions are actually lower limits, because dark matter is implicitly included in dynamical mass estimates and molecular hydrogen ignored. Hence, it is found useful to calculate upper limits using M/L estimates from starburst evolutionary models. For most objects, very extreme upper limits have to be used, assuming the galaxies to experience maximum luminosity of their first burst, except for three galaxies where the known star formation histories allow us to adopt more moderate and realistic upper limits. If star formation histories are found for a larger sample of dIrrs and even BCGs constraining chemical evolution models with observed gas fraction intervals may eventually turn out to be extremely useful. The closed models do not reproduce the gas fractions of the three well-known objects, even if a lower IMF-cutoff, equal to $0.01 M_{\odot}$ instead of $0.1 M_{\odot}$ is adopted. Hence, open models are considered, allowing gas to escape or to accrete on to the galaxy. Two kind of winds, enriched and ordinary, have been used. The results when incorporating enriched winds are not in accordance with the observed level of N/O and the Y-O/H fitting is not satisfactory, when the gas fractions of the three well-known systems are fitted. Hence, it is concluded that our models employing enriched winds is in conflict with the observations.

The next step is to include ordinary instead of enriched winds. Both N/O-O/H and Y-O/H are fitted, with results resembling those of the closed model. Unfortunately, only the gas fraction of one of the three selected galaxies is fitted, not differing much from the results of the closed model. To check the inclusion of ordinary winds, the outcome of the model is compared to the results of a simple analytical model, employing continuous star formation. A close resemblance is found between the two models at low metallicities, but at higher metallicities, the numerical model seems to have problems in getting the yield down. The difference may be caused by the behavior of starbursts at a low absolute gas mass. This is confirmed when comparing the numerical model, changed slightly to employ continuous star formation, to the analytical model, displaying almost identical outputs. Thus, it is concluded that it is important to specify clearly whether instantaneous bursts or continuous star formation is used, when including ordinary winds. Instantaneous bursts resemble the intense bursts of BCGs, whereas

the more moderate bursts of dIrrs are better explained using a continuous SFR.

Finally, inflow and ordinary winds were included. The results are in accordance with all observations, except that it is difficult to obtain the right gas fractions and N/O scatter simultaneously. Only for quite extreme parameter choices as in fig. 23 and 24, one may be successful. It may be important to note that the results, when using the combined inflow/ordinary wind model, show the upturn in N/O to be more pronounced, than it was for the closed model.

One question is unavoidable: which model is preferred? It is impossible to give an unambiguous answer. Dwarf galaxies are different, both in mass and appearance. Some are explained well by a closed model, others need a combination of ordinary winds and inflow. This is true for both dIrrs and BCGs. However, for dIrrs one should prefer to adopt a more continuous SFR before fitting the observations.

In all cases, the model including enriched winds seems to be ruled out, since it is in direct conflict with the observations, as also found by e.g. Carigi et al. (1999).

REFERENCES

- Allouin D., Collin-Souffrin S., Joly M., Vigroux L., 1979, *A&A*, 78, 200
- Brinks E., Klein U., 1988, *MNRAS*, 231, 63
- Carigi L., Colin P., Peimbert M., Sarmiento A., 1995, *ApJ*, 445, 98
- Carigi L., Colín P., Peimbert M., 1999, *ApJ*, 514, 787
- Charlot S., Bruzual G., 1991, *ApJ*, 367, 126
- Edmunds M.G., Pagel B.E.J., 1978, *MNRAS*, 185, 77
- Elmegreen B. G., 1994, *ApJ*, 427, 384
- Franco J., Ferrara A., Rózyżczka M., Tenorio-Tagle G., Cox D.P., 1993, *ApJ*, 407, 100
- Gallart C., Aparicio A., Bertelli G., Chiosi C., 1996, *AJ*, 112, 2596
- Garnett D. R., 1990, *ApJ*, 363, 142
- Geha et al., 1998, *AJ*, 115, 1045
- Gerola H., Seiden P.E., Schulman L.S., 1980, *ApJ*, 242, 517
- Hartwick F. D. A., 1976, *ApJ*, 209, 418
- Izotov Y. I., Thuan T. X., 1998, *ApJ*, 497, 227
- Izotov Y. I., Thuan T. X., Lipovetsky V. A., 1997a, *ApJS*, 108, 1
- Izotov Y. I., Lipovetsky V. A., Chaffee F. H., Foltz C. B., Guseva N. G., Kniazev A. Y., 1997b, *ApJ*, 476, 698
- Kennicutt R. C., 1984, *ApJ*, 287, 116
- Kobulnicky C., 1997, preprint, astro-ph/9711077
- Kobulnicky H. A., Skillman E. D., 1996, *ApJ*, 471, 211
- Kobulnicky H. A., Skillman E. D., 1997, *ApJ*, 489, 636
- Kobulnicky H. A., Skillman E. D., 1998, *ApJ*, 497, 601
- Kumai Y., Tosa M., 1992, *A&A*, 257, 511
- Kunth D., Sargent W. L. W., 1986, *ApJ*, 300, 496
- Lacey C. G., Fall S. M., 1985, *ApJ*, 290, 154
- Leitherer C. in ASP Conference Series vol. 142: *The Stellar Initial Mass Function*, Gilmore G., Howell D.(eds.), p. 61
- Leitherer C., Heckman, T. M., 1995, *ApJS*, 96, 9
- Lequeux J., Peimbert M., Rayo J. F., Serrano A., Torres-Peimbert S., 1979, *A&A*, 80, 155
- Lu L., Sargent W. L. W., Barlow T. A., 1998, *AJ*, 115, 55
- Mac Low M.-M., McCray R., 1988, *ApJ*, 324, 776
- McCray R., Kafatos M., 1987, *ApJ*, 317, 190
- Maeder A., 1992, *A&A*, 264, 105
- Marconi G., Matteucci F., Tosi M., 1994, *MNRAS*, 270, 35
- Marigo, P., 1998, *A&A*, 340, 463
- Marigo P., Bressan A., Chiosi C., 1996, *A&A*, 313, 545
- Marigo P., Bressan A., Chiosi C., 1998, *A&A*, 1998, 331,564
- Marlowe A. T., Heckman T. M., Wyse R. F. G., Schommer R., 1995, *ApJ*, 438, 563
- Martin C., 1998, *ApJ*, 506, 222
- Massey P. in ASP Conference Series vol. 142: *The Stellar Initial Mass Function*, Gilmore G., Howell D.(eds.), p. 17
- Matteucci F., Chiosi C., 1983, *A&A*, 123, 121
- Matteucci, F. and Tosi, M., 1985, *MNRAS*, 217, 391
- Matteucci F., Molaro P., Vladilo G., 1997, *A&A*, 321, 45
- Meurer G. R., 1998, in *Dwarf galaxies and cosmology*, Thuan T. X., Balkowski C., Cayatte V., Tran Than Van J. (eds.), Edition Frontieres, in press
- Mori M., Yoshii Y., Tsujimoto T., Nomoto K., 1997, *ApJ*, 478, L21
- Osterbrock D. E., 1989, *Astrophysics of gaseous nebulae and active galactic nuclei*, University Science Books
- Pagel B. E. J., 1997, *Nucleosynthesis and chemical evolution of galaxies*, Cambridge University Press
- Pagel B. E. J., Patchett B. E., 1975, *MNRAS*, 172, 13
- Pagel B. E. J., Tautvaišėnė G., 1998, *MNRAS*, 299, 535
- Pagel B. E. J., Simonson E. A., Terlevich R. J., Edmunds M. G., 1992, *MNRAS*, 255, 325
- Peimbert M., 1978, in IAU Symp. 84: *The Large-Scale Characteristics of the Galaxy*, Burton W.B. (ed.), Reidel
- Pettini M., Lipman K., Hunstead R.W., 1995, *ApJ*, 451, 100
- Pilyugin L. S., *A&A*, 1992, 260, 58
- Pilyugin L. S., *A&A*, 1993, 277, 42
- Portinari L., Chiosi C., Bressan A., 1998, *A&A*, 334, 505
- Renzini A., Voli M., 1981, *A&A*, 94, 175
- Salpeter E. E., 1955, *ApJ*, 121, 161
- Schaller G., Schaerer D., Meynet G., Maeder A., 1992, *A&AS*, 96, 269
- Searle L., Sargent W. L. W., 1971, *ApJ*, 173, 25
- Searle L., Sargent W.L.W., Bagnuolo W.G., 1973, *ApJ*, 179, 427
- Silich S. A., Tenorio-Tagle G., 1998, *MNRAS*, 299, 249
- Smith, E., 1975, *ApJ*, 199, 591
- Sommer-Larsen J., Antonuccio-Delogu V., 1993, *MNRAS*, 262, 350
- Spitzer L. Jr., 1978, *Physical processes in the interstellar medium*, Wiley, p.105, 246
- Stasinska G., Leitherer C., 1996, *ApJS*, 107, 661
- Staveley-Smith L., Davies R. D., Kinman T. D., 1992, *MNRAS*, 258, 334
- Taylor C. L., Brinks E., Pogge R. W., Skillman, E. D., 1994, *AJ*, 107, 971
- Tenorio-Tagle G., 1996, *AJ*, 111, 1641
- Thuan T. X., Martin G. E., 1981, *ApJ*, 247, 823
- Thuan T. X., Izotov Y. I., Lipovetsky V. A., 1996, *ApJ*, 463, 120
- Tomisaka K., Habe H., Ikeuchi S., 1981, *Ap&SS*, 78, 237
- van den Hoek L. B., Groenewegen M. A. T., 1997, *A&AS*, 123, 305
- van Zee L., Salzer J.J., Haynes M. P., 1998, *ApJ*, 497, L1
- van Zee L., Westpfahl D., Haynes M. P., 1998, *AJ*, 115, 1000
- Vila-Costas M.B., Edmunds M.G., 1993, *MNRAS*, 265, 199
- Woolsey S. E., Weaver T. A., 1986, *ARA&A*, 24, 205
- Woolsey S. E., Weaver T. A., 1995, *A&AS*, 101, 181
- Wyse R. F. G. in ASP Conference Series vol. 142: *The Stellar Initial Mass Function*, Gilmore G., Howell D.(eds.), p. 89